ChromaTech: A discontinuous Galerkin spectral element simulator for preparative liquid chromatography

Kristian Meyer[a,b,*], Samuel Leweke[c,d], Eric von Lieres[c], Jakob K. Huusom[b], Jens Abildskov[b]

[a]Meyer Chroma Technology (MCT) ApS, Hollandsvej 5, DK-2800 Kgs. Lyngby, Denmark
[b]Technical University of Denmark, Process and Systems Engineering Center (PROSYS), Department of Chemical and Biochemical Engineering, Building 229, DK-2800, Kgs. Lyngby, Denmark
[c]Forschungszentrum Jülich, IBG-1: Biotechnology, 52428 Jülich, Germany
[d]University of Cologne, Mathematical Institute, Weyertal 86-90, 50931 Köln, Germany

Abstract

ChromaTech is a simulator for preparative liquid chromatography processes with mass transport described by the pore and surface diffusion general rate model. A discontinuous Galerkin spectral element method is used for spatial discretization with exponential decay of approximation errors within elements. The code is validated by numerically reproducing a high-precision reference obtained with CADET-semi-analytic. The performance of ChromaTech is tested by comparing against CADET, a dedicated code based on a weighted essentially non-oscillatory finite volume method with second (low) order spatial accuracy. Reassuringly, ChromaTech provides exactly the same chromatograms as CADET for multicomponent protein purification cases with linear and non-linear adsorption dynamics. However, the numerical results show, that ChromaTech has superior efficiency in terms of computational cost and discrete problem size without compromising stability. The spatial discretization is the major difference between the two codes for solution of the pore and surface diffusion general rate model. Thus, it demonstrates, that spectral methods are not just competitive with second (low) order accurate methods often used by default, but simply a superior approach for spatial discretization of liquid chromatography flow problems in terms of computational efficiency.

Keywords: High-order; Discontinuous Galerkin Spectral element method; Liquid chromatography; Steric-mass-action isotherm; General rate model; Parallel pore/surface diffusion

1. Introduction

Biopharmaceuticals provide important therapeutic options for many serious clinical conditions (Sanchez-Garcia et al., 2016). Unfortunately, access to these products remains a significant problem for patients. That is often because of high treatment cost (Kozlowski et al., 2011; Monk et al., 2017; Cherny et al., 2016), e.g. a monoclonal antibody treatment for cancer can cost up to $35,000 annually per patient (Farid, 2007).

Today, it is globally accepted to develop biopharmaceticals that are similar to a reference product (biosimilars) to reduce drug prices (Cazap et al., 2018). With the blossoming of the biosimilar market (Walsh, 2018), biopharmaceutical companies are challenged by increased economical pressure from biosimilars (Ahmed et al., 2012). Therefore, reduction of production cost is likely to gain importance relative to speed-to-market as the main market driver (Nfor et al., 2009).

The production costs are typically dominated by downstream bioprocessing (McGlaughlin, 2012). Here, liquid chromatography columns operated in batch-mode are core unit operations used to recover and purify biopharmaceuticals from complex fermentation broth. It seems unlikely that it will lose its place in biomanufacturing in the foreseeable future (Hanke and Ottens, 2014).

In industry, chromatography columns are typically operated based on robust and fixed manufacturing schedules (Close et al., 2014) without feedback control and plant-wide coordination. This causes a loss of performance that can potentially be avoided, by adjusting the process with inputs that are on-time and that are optimized, based on on-line measurements. Model predictive control is used to reduce production costs in other industries where efficient manufacturing has been important for decades (Lee, 2011; Huusom, 2015), e.g. for manufactures that uses distillation columns (Meyer et al., 2017).

Recently, the benefits of plant-wide process control for biomanufacturing has been demonstrated in small-scale equipment (Gomis-Fons et al., 2020; Feidl et al., 2020). Moreover, the benefits of model predictive control have been demonstrated for several chromatographic systems, see e.g. Papathanasiou et al. (2017); Engell (2007). However, the solution of optimal control problems constrained by non-linear chromatographic models is computationally

*Corresponding Author. Tel.: +45 91824054
Email address: km@meyerct.com (Kristian Meyer)

demanding (Holmqvist and Magnusson, 2016), especially if combined with non-linear state estimation such as the extended Kalman filter to handle process uncertainty and plant-model mismatch (Hørsholt et al., 2019a,b). Other relevant numerical challenges arise for e.g. Bayesian inference applications (Briskot et al., 2019), process synthesis of detailed flow-sheets (Pirrung et al., 2017, 2019), simulation of 2D general rate models (Qamar et al., 2017), and for simulation of chromatography models with inhomogeneous resin beads (Gerontas et al., 2013; Püttmann et al., 2014).

Thus, the current digitalization of biomanufacturing processes (Nargund et al., 2019) can benefit from more efficient algorithms to solve non-linear mechanistic-type process models. For this reason, ChromaTech (Meyer Chroma Technology ApS, Technical University of Denmark) (Meyer, 2020) has been developed. In this work, the attention will be on batch chromatography, although the presented method can be extended to e.g. continuous chromatographic systems (Rathore et al., 2018).

ChromaTech is based on a discontinuous Galerkin spectral element method in nodal form (Hesthaven and Warburton, 2002, 2008), that allows arbitrary high-order (spectral) convergence within elements while retaining stability of the method (Meyer et al., 2018b, 2019). Moreover, the method is mass-conservative and can be naturally extended to support mesh refinement with adaptive element sizes and polynomial orders (hp-adaptivity), see e.g. Palm et al. (2017). The discontinuous Galerkin method can be considered a high-order generalization of the finite volume method (Dumbser et al., 2008).

A multi-element formulation is used to discretize the convection-dominated mobile phase flow to localize steep concentration fronts within elements. The purely diffusive flow in the pore phase is discretized within a single-element domain with global spectral convergence rate.

Such spectral methods are in general gaining prominence in science and engineering over traditional methods with second (low) order spatial accuracy due to improved accuracy at reduced computational costs (Xu et al., 2018). However, their use is often limited by their complexity, which makes them challenging to implement and use. ChromaTech encloses the mathematical complexities of these methods in efficient C++ routines, with the aim of making them accessible to the biomanufacturing industries.

Here, the objective is to demonstrate the computational benefits of using spectral discontinuous Galerkin methods compared to second (low) order methods often used by default for spatial discretization of chromatography models. The performance is measured in terms of computational cost and discrete problem size (i.e. the length of the state-vector) while stability must be retained. A small discrete problem size is beneficial since a smaller system has to be stored and integrated in time. Moreover, it is beneficial for non-linear state estimation (Hørsholt et al., 2019a).

The Chromatography Analysis and Design Toolkit (CADET) (Jülich Research Center) (von Lieres and Andersson, 2010; Püttmann et al., 2013; Leweke and von Lieres, 2018) is used for benchmark comparisons. It is based on a second (low) order accurate weighted essentially non-oscillatory finite volume method typically used due to strong built-in stability properties. It is well suited as a benchmark, since its C++ implementation has been optimized over long development time lines. Moreover, it is the only chromatography simulator that is open source and free of charge with unlimited functionality enabling us to extract relevant information for benchmarking purposes. Such information is often difficult to extract from commercial products such as Aspen Chromatography (AspenTech), Virtual Column (Dionex), Chrom Works (YpsoFacto), ChromX (GoSilico) and Chromulator (Ohio University). Finally, the major difference between ChromaTech and CADET is the spatial discretization procedure, enabling us to compare different strategies.

This paper is organized as follows: Section two presents the pore and surface diffusion general rate model. In section three, the numerical solution procedure used in ChromaTech is described and its implementation is compared with CADET. Section four presents an analytical solution technique which is used to validate correct implementation of ChromaTech in section five. Additionally, section five presents benchmark comparisons of ChromaTech against CADET. Finally, concluding remarks are collected in section six.

2. The chromatography model

In this section, the governing equations are given for the pore and surface diffusion general rate model (Costa and Rodrigues, 1985a,b; Ma et al., 1996; Schmidt-Traub et al., 2012) with ion-exchange adsorption (Brooks and Cramer, 1992). The model accounts for axial mass transport by forced convection and dispersion in the mobile phase percolating through the column, mass transport from the mobile phase through the laminar boundary layer surrounding the porous column particles (beads) by film diffusion, and mass transport inside the particle pore system by pore and surface diffusion. A conceptual illustration of the mass transport phenomena and the ion-exchange adsorption process involved is given in Fig. 1.

2.1. Mass transport in the mobile phase

The mass balance for the mobile phase (the interstitial column volume) is given by (Schmidt-Traub et al., 2012)

$$\frac{\partial c_i}{\partial t}(z,t) = -\frac{\partial f_i}{\partial z}(z,t) - F_c \frac{3}{R_p} j_i(z,t)\,, \tag{1a}$$

$$f_i(z,t) = v_{\text{int}} c_i(z,t) - D_{\text{ax}} \frac{\partial c_i}{\partial z}(z,t)\,, \tag{1b}$$

$$j_i(z,t) = k_{\text{film},i}\left(c_i(z,t) - c_{p,i}(z,t)\Big|_{r=R_p}\right), \tag{1c}$$

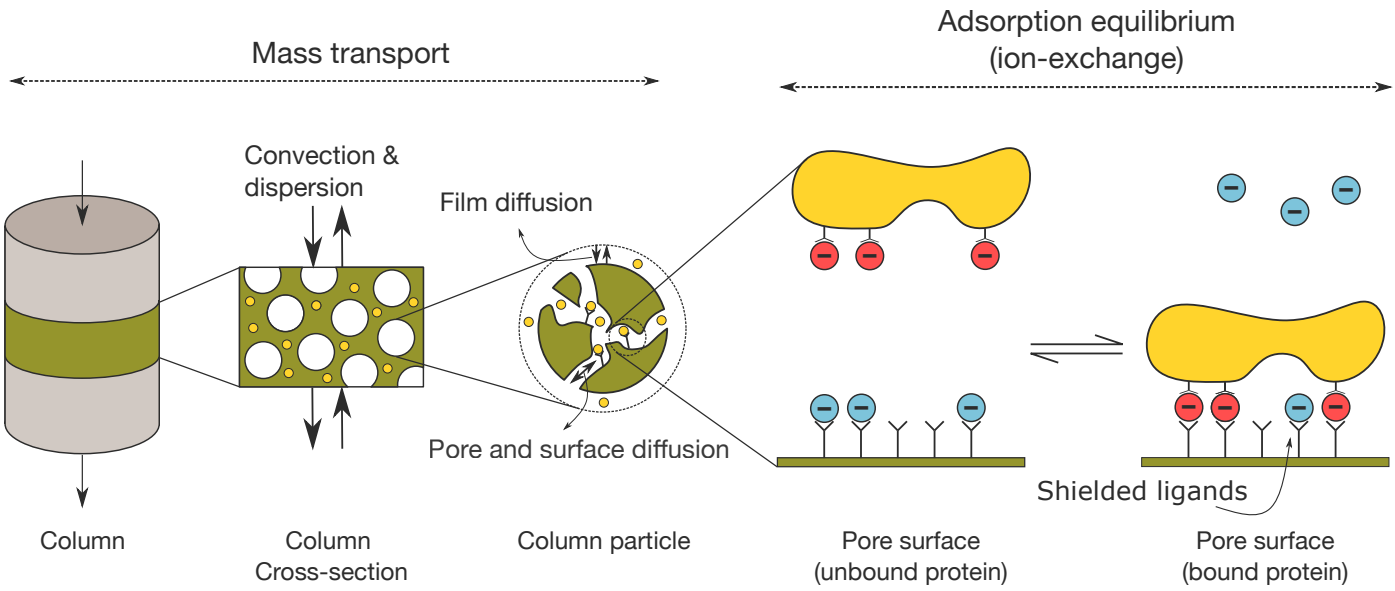

Figure 1: Conceptual illustration of the transport phenomena included in the pore and surface diffusion general rate model and of the ion-exchange adsorption processes to ligands attached to the inside of the porous particles.

for all the components $i \in [0, N_c]$. Here, $i = 0$ represents the salt component, and $i = 1, \ldots, N_c$ represents N_c proteins. Moreover, c_i and $c_{p,i}$ are the (unbound) mobile phase and pore phase concentrations, respectively, f_i are mobile phase convective-dispersive fluxes, v_{int} is the interstitial velocity, D_{ax} is the axial dispersion coefficient, $F_c = (1 - \varepsilon_c)/\varepsilon_c$ is the column phase ratio, ε_c is the column porosity, R_p is the radius of the porous particles, j_i are fluxes from the mobile phase into the pore phase, and $k_{\text{film},i}$ are film mass transfer coefficients. Additionally, $z \in \Omega_z = [0, L]$ is the axial position in the axial domain Ω_z, L is the column length, $t \in [0, \infty)$ is the time variable, $r \in \Omega_r = [0, R_p]$ is the position along the radius of the porous particles in the radial domain Ω_r.

2.2. Mass transport in the pore phase

The mass balance for the pore phase (the pore volume) is modelled as Fick's diffusion in spherical coordinates (Schmidt-Traub et al., 2012). It is given by

$$\left(\frac{\partial c_{p,i}}{\partial t}(z,r,t) + F_p \frac{\partial q_i}{\partial t}(z,r,t)\right) = \frac{1}{r^2}\frac{\partial}{\partial r}\left[r^2\left(D_{\text{p},i}\frac{\partial c_{p,i}}{\partial r}(z,r,t) + D_{\text{s},i}F_p\frac{\partial q_i}{\partial r}(z,r,t)\right)\right], \tag{2}$$

for all the components $i \in [0, N_c]$. Here, $D_{p,i}$ and $D_{s,i}$ are pore and surface diffusion coefficients, respectively, $F_p = (1-\varepsilon_p)/\varepsilon_p$ is the particle phase ratio, ε_p is the particle porosity, q_0 is the (bound) stationary phase concentration of salt counter-ions, and q_i, $i = 1, \ldots, N_c$ are (bound) stationary phase concentrations of proteins.

2.3. Adsorption isotherm

Assuming that the stationary phase salt counter-ions that are accessible for exchange q_0^{acc} are monovalent, the ion-exchange stoichiometric scheme is

$$c_{p,i} + \nu_i q_0^{\text{acc}} \Leftrightarrow q_i + \nu_i c_{p,0}, \quad \forall i = 1, \ldots, N_c\,, \tag{3}$$

where ν_i are characteristic charges of the adsorbing proteins. The concentration of accessible salt counter-ions are calculable from the electroneutrality condition

$$\Lambda = q_0^{\text{acc}} + \sum_{j=1}^{N_c}\left(\sigma_j + \nu_j\right)q_j\,, \tag{4}$$

where Λ is the ionic capacity, and σ_i are the number of inaccessible (shielded) binding sites due to the ith adsorbed protein. The total salt concentration is

$$q_0 = q_0^{\text{acc}} + \sum_{j=1}^{N_c}\sigma_j q_j = \omega_0\,. \tag{5}$$

The thermodynamic equilibrium constant $K_{\text{eq},i}$ for the stoichiometric scheme Eq. (3) is defined in terms of concentrations by (Atkins and de Paula, 1998)

$$K_{\text{eq},i} = \frac{q_i}{c_{p,i}}\left(\frac{c_{p,0}}{q_0^{\text{acc}}}\right)^{\nu_i}\,, \tag{6}$$

where it is assumed that none of the involved components contribute to non-ideal behaviour of the mixture. Combining Eqs. (6) and (4) gives the steric-mass-action isotherm (Brooks and Cramer, 1992)

$$q_i = c_{p,i}A_i\left(1 - \sum_{j=1}^{N_c}\frac{q_j}{q_{\max,j}}\right)^{\nu_i} = \omega_i\,, \tag{7}$$

where $A_i = K_{\text{eq},i}\left(\Lambda/c_{p,0}\right)^{\nu_i}$ are initial isotherm slopes, and $q_{\max,j} = \Lambda/(\sigma_i + \nu_i)$ are maximum binding capacities.

For dilute systems, the stationary phase concentrations are much lower compared to the capacities, i.e. $q_i \ll q_{\max,i}$, $i = 1, \ldots, N_c$. Then, Eq. (7) simplifies for the ith component to the linear isotherm

$$q_i \approx c_{p,i} A_i \,. \tag{8}$$

2.4. Boundary conditions and initial values

To complete the model, appropriate boundary and initial conditions are specified. Danckwerts boundary conditions (Danckwerts, 1953) are applied at the column inlet and outlet. The inlet Robin conditions are given by

$$f_i(t)|_{z=0} = v_{\text{int}} c_{\text{inj},i}(t), \quad \forall i \in [0, N_c] \,, \tag{9}$$

such that the injected fluxes $v_{\text{int}} c_{\text{inj},i}(t)$ are dispersed immediately upon entering the column. For simplicity, a rectangular injection profile can be assumed, i.e.

$$v_{\text{int}} c_{\text{inj},i}(t) = \begin{cases} v_{\text{int}} c_{\text{f},i}, & 0 \leq t \leq t_{\text{inj}}, \\ 0, & t > t_{\text{inj}} \,, \end{cases} \tag{10}$$

for all the proteins $i \in [1, N_c]$. Here, $c_{\text{f},i}$ are protein feed concentrations and t_{inj} is the injection time. The salt injection profile $c_{\text{inj},0}$ can be chosen to manipulate the equilibrium conditions in the column using e.g. step or gradient profiles. Neumann conditions are used on the column outlet

$$\left.\frac{\partial c_i}{\partial z}(t)\right|_{z=L} = 0, \quad \forall i \in [0, N_c] \,, \tag{11}$$

such that the concentration does not change after leaving the column. At the particle surface, the following flux boundary conditions are used:

$$\begin{aligned} D_{p,i} \left.\frac{\partial c_{p,i}}{\partial r}(z,t)\right|_{r=R_p} + F_p D_{s,i} \left.\frac{\partial q_i}{\partial r}(z,t)\right|_{r=R_p} \\ = \frac{j_i(z,t)}{\varepsilon_p}, \quad \forall i \in [0, N_c] \,. \end{aligned} \tag{12}$$

Due to symmetry, Neumann conditions are used at the center of the particles, i.e.

$$\left.\frac{\partial c_{p,i}}{\partial r}(z,t)\right|_{r=0} = 0, \quad \forall i \in [0, N_c] \,. \tag{13}$$

The mobile phase concentrations representing a column which is initially empty from proteins and equilibrated with running salt buffer are given by

$$c_i(z)|_{t=0} = 0, \quad \forall i \in [1, N_c] \,, \tag{14a}$$

$$c_0(z)|_{t=0} = c_{0,\text{init}} \,, \tag{14b}$$

where $c_{0,\text{init}}$ is the salt concentration of the buffer used to equilibrate the column. Initial pore phase concentrations representing particles that are equilibrated are given by

$$\left.c_{p,i}(z,r)\right|_{t=0} = 0, \quad \forall i \in [1, N_c] \,, \tag{15a}$$

$$\left.c_{p,0}(z,r)\right|_{t=0} = c_{0,\text{init}} \,. \tag{15b}$$

Finally, the stationary phase concentrations for initially equilibrated particles are

$$q_i(z,r)|_{t=0} = 0, \quad \forall i \in [1, N_c] \,, \tag{16a}$$

$$q_0(z,r)|_{t=0} = \Lambda \,, \tag{16b}$$

such that the electroneutrality condition is fulfilled.

3. Numerical solution techniques used in ChromaTech

In this section, the numerical techniques used in ChromaTech to solve the chromatography model are given. A method of lines approach is considered. The spatial differential operators are discretized first resulting in a semi-discrete system (discrete in space, continuous in time) of differential algebraic equations to be integrated in time from consistent initial conditions.

3.1. The standard nodal element

A standard nodal element (Hesthaven and Warburton, 2002, 2008) is constructed with reference region $I = [-1, 1]$ and reference variable $\xi \in I$. The core element-level operations are implemented on this standard element, such that only one set of operators has to be stored.

The numerical approximation y_h to the exact solution y can be expressed through a polynomial dual interpolation of the form

$$y(\xi, t) \approx y_h(\xi, t) = \sum_{m=1}^{N_p} y_h(t)|_{\xi_m} \, l_m(\xi) = \sum_{m=1}^{N_p} \hat{y}_m(t) \tilde{P}_{m-1}(\xi) \,, \tag{17}$$

which is valid provided that the grid nodes $\{\xi_m\}_{m=1}^{N_p}$ are distinct. Here, $\hat{y}_m$ are interpolatory expansion coefficients, $\tilde{P}_{m-1}$ are orthonormal Legendre polynomials, and l_m are Lagrange interpolating polynomials defined in terms of the N_p distinct grid nodes ξ_m with cardinal property $l_n(\xi_m) = \delta_{nm}$ (δ_{nm} is the Kronecker delta). The grid nodes $\{\xi_n\}_{n=1}^{N_p}$ are chosen as the Legendre-Gauss-Lobatto quadrature (the Fekete/Fejér) nodes since this set is near-optimal in terms of the Lebesgue constant (Hesthaven, 1998) and includes the interval boundaries.

The non-singular generalized Vandermonde matrix $\mathcal{V}$ with elements $\mathcal{V}_{nm} = \tilde{P}_{m-1}(\xi_n)$ can be used to relate the interpolatory expansion coefficients $\hat{y}_m$ to the nodal coefficients $y(\xi_m)$ by

$$\boldsymbol{y}_h = \mathcal{V} \hat{\boldsymbol{y}} \,, \tag{18}$$

where

$$\boldsymbol{y}_h = \left[y_h(t)|_{\xi_1}, \ldots, y_h(t)|_{\xi_{N_p}} \right]^\mathsf{T} \,, \tag{19}$$

is a vector of nodal coefficients, and

$$\hat{\boldsymbol{y}} = \left[\hat{y}_1(t), \ldots, \hat{y}_{N_p}(t) \right]^\mathsf{T} \,, \tag{20}$$

is a vector of interpolatory expansion coefficients. Moreover, it expresses the Lagrange interpolating polynomials in terms of the orthonormal Legendre polynomials

$$\mathcal{V}^\mathsf{T} \boldsymbol{l} = \tilde{\boldsymbol{P}} \,, \tag{21}$$

where

$$\boldsymbol{l} = \left[l_1(\xi), \ldots, l_{N_p}(\xi)\right]^\mathsf{T} , \tag{22}$$

is a vector of Lagrange interpolating polynomials and

$$\tilde{\boldsymbol{P}} = \left[\tilde{P}_0(\xi), \ldots, \tilde{P}_N(\xi)\right]^\mathsf{T} , \tag{23}$$

is a vector of orthonormal Legendre polynomials of order at most $N = N_p - 1$.

Choosing a nodal representation, the following matrices are needed to design spectral methods

$$\mathcal{M}_{nm} = \int_{-1}^{1} l_n(\xi) l_m(\xi) \mathrm{d}\xi, \qquad \mathcal{M} = (\mathcal{V}\mathcal{V}^\mathsf{T})^{-1} , \tag{24a}$$

$$\mathcal{S}_{nm} = \int_{-1}^{1} l_n(\xi) \frac{dl_m}{\mathrm{d}\xi}(\xi) \mathrm{d}\xi, \qquad \mathcal{S} = \mathcal{M}\mathcal{D}, \tag{24b}$$

where orthonormality of the basis functions is exploited instead of using a quadrature rule to calculate the integrals. Here, $\mathcal{M}$ is the nodal mass matrix, $\mathcal{S}$ is the nodal first-order stiffness matrix and the differentiation matrix $\mathcal{D}$ has element values

$$\mathcal{D}_{nm} = \left.\frac{\mathrm{d}l_m}{\mathrm{d}\xi}\right|_{\xi_n} . \tag{25}$$

It is calculable as

$$\mathcal{D} = \mathcal{V}_\xi \mathcal{V}^{-1}, \quad \mathcal{V}_{\xi,(nm)} = \left.\frac{\mathrm{d}\tilde{P}_{m-1}}{\mathrm{d}\xi}\right|_{\xi_n} . \tag{26}$$

Moreover, the lifting matrix $\mathcal{L}$ is introduced to compute surface integrals,

$$\mathcal{L} = \mathcal{M}^{-1}\mathcal{E}, \quad \mathcal{E}_{i,1} = l_i(-1), \quad \mathcal{E}_{i,2} = l_i(1) , \tag{27}$$

where $\mathcal{E}$ is a zero matrix with $\mathcal{E}_{1,1} = 1$ and $\mathcal{E}_{N_p,2} = 1$ due to the property $l_n(\xi_m) = \delta_{nm}$.

Alternatively, the interpolant y_h can be expressed as

$$y_h(\xi, t) = \sum_{m=1}^{N_p} y_h(t)|_{\xi_m} \, l_m(\xi) = \sum_{m=1}^{N_p} \hat{y}_m(t) \tilde{P}^{(0,2)}_{m-1}(\xi) , \tag{28}$$

where $\tilde{P}^{(0,2)}_{m-1}$ are orthonormal Jacobi polynomials with weight function $w = (1+\xi)^2$. Using this formulation, the following matrices can be computed exactly by exploiting the weighted orthonormality of the basis:

$$\begin{aligned} \mathcal{M}^{(0,2)}_{nm} &= \int_{-1}^{1} l_n(\xi) l_m(\xi) (1+\xi)^2 \mathrm{d}\xi, \\ \mathcal{M}^{(0,2)} &= \left(\mathcal{V}^{(0,2)} \left(\mathcal{V}^{(0,2)}\right)^\mathsf{T}\right)^{-1} , \end{aligned} \tag{29a}$$

$$\begin{aligned} \mathcal{A}^{(0,2)}_{nm} &= \int_{-1}^{1} \frac{\mathrm{d}l_n}{\mathrm{d}\xi}(\xi) \frac{\mathrm{d}l_m}{\mathrm{d}\xi}(\xi) (1+\xi)^2 \mathrm{d}\xi, \\ \mathcal{A}^{(0,2)} &= \left(\mathcal{D}^{(0,2)}\right)^\mathsf{T} \mathcal{M}^{(0,2)} \mathcal{D}^{(0,2)} , \end{aligned} \tag{29b}$$

leaving the implementation quadrature-free. Here, $\mathcal{M}^{(0,2)}$ is a weighted nodal mass matrix, $\mathcal{A}^{(0,2)}$ is a weighted nodal second-order stiffness matrix, $\mathcal{V}^{(0,2)}$ is a non-singular generalized Vandermonde matrix with elements $\mathcal{V}^{(0,2)}_{nm} = \tilde{P}^{(0,2)}_{m-1}(\xi_n)$, and the differentiation matrix $\mathcal{D}^{(0,2)}$ is computed using

$$\mathcal{D}^{(0,2)} = \mathcal{V}^{(0,2)}_\xi \left(\mathcal{V}^{(0,2)}\right)^{-1}, \quad \mathcal{V}^{(0,2)}_{\xi,(nm)} = \left.\frac{\mathrm{d}\tilde{P}^{(0,2)}_{m-1}}{\mathrm{d}\xi}\right|_{\xi_n} . \tag{30}$$

Finally, the weighted lifting matrix $\mathcal{L}^w$ is introduced as

$$\mathcal{L}^{(0,2)} = \left(\mathcal{M}^{(0,2)}\right)^{-1} \mathcal{E} . \tag{31}$$

3.2. Spatial discretization in the axial direction

In this section, the axial differential operators in Eq. (1) are discretized using a discontinuous Galerkin spectral element method.

3.2.1. The computational domain

The computational domain Ω_z is divided into N_e non-overlapping axial elements Ω^k_z, such that $\Omega_z = \bigcup_{k=1}^{N_e} \Omega^k_z$. Each Ω^k_z is mapped to the standard element by an affine mapping

$$\xi^k_z(z) = \frac{2\left(z - z^k_L\right)}{\Delta z^k} - 1 , \tag{32}$$

where $\Delta z^k = z^k_R - z^k_L$ is the element size of Ω^k_z, z^k_L and z^k_R are the left and right edges of Ω^k_z, respectively, and $\mathcal{J}^k_z = 2/\Delta z^k$ is Jacobian of the affine mapping.

3.2.2. General formulation

To apply the discontinuous Galerkin spectral element method on second order differential operators, the approach of Bassi and Rebay (1997) is used. That is, Eq. (1) is rewritten as an equivalent first order system to give for the ith component

$$\frac{\partial c_i}{\partial t} = -\frac{\partial h_i}{\partial z} - F_c \frac{3}{R_p} j_i , \tag{33a}$$

$$g_i = \sqrt{D_{\mathrm{ax}}} \frac{\partial c_i}{\partial z} , \tag{33b}$$

where g_i are gradient variables and $h_i = v_{\mathrm{int}} c_i - \sqrt{D_{\mathrm{ax}}} g_i$ are mobile phase fluxes.

The starting point is to cast Eq. (33) in a finite-dimensional weak form by multiplying (33) by test functions $v^z_h \in \mathbb{V}^z_h$, integrating over the domain Ω_z, and finally performing integration by parts. In spectral element methods, the approximate solutions $c_{h,i}$ and g_{h_i} to the exact functions c_i and g_i, respectively, are chosen to belong to a finite-dimensional trial space $\mathbb{U}^z_h$. The finite dimensional spaces of trial $\mathbb{U}^z_h$ and test $\mathbb{V}^z_h$ functions are chosen to coincide according to the Galerkin method. To obtain a discontinuous Galerkin method, these spaces are chosen to be broken spaces. That is

$$\mathbb{U}^z_h = \mathbb{V}^z_h = \bigoplus_{k=1}^{N_e} \mathbb{V}^k_h = \bigoplus_{k=1}^{N_e} \mathrm{span}\left\{\left(l_m \circ \xi^k_z\right)\right\}_{m=1}^{N^z_p} , \tag{34}$$

where the local finite dimensional spaces $\mathbb{V}_h^k$ are populated with Lagrange interpolating polynomials l_m of degree at most $N^z = N_p^z - 1$ giving a nodal method.

Since $\mathbb{V}_h^z$ is a broken space, a strictly local finite-dimensional weak form can be considered. It can be expressed for the ith component, and for the kth axial element as follows: find $u_h \in \mathbb{V}_h^k$ and $g_h \in \mathbb{V}_h^k$ such that

$$\begin{aligned}\int_{\Omega_z^k} \frac{\partial c_{h,i}}{\partial t} l_m^k \mathrm{d}z = &\int_{\Omega_z^k} h_{h,i} \frac{\partial l_m^k}{\partial z} \mathrm{d}z - \int_{\partial\Omega_z^k} \hat{\boldsymbol{n}} h_{h,i} l_m^k \mathrm{d}z \\ &- F_c \frac{3}{R_p} \int_{\Omega_z^k} j_{h,i} l_m^k \mathrm{d}z \,,\end{aligned} \tag{35a}$$

$$\begin{aligned}\int_{\Omega_z^k} g_{h,i} l_m^k \mathrm{d}z = &-\sqrt{D_{\mathrm{ax}}} \int_{\Omega_z^k} c_{h,i} \frac{\partial l_m^k}{\partial z} \mathrm{d}z \\ &+ \sqrt{D_{\mathrm{ax}}} \int_{\partial\Omega_z^k} \hat{\boldsymbol{n}} c_{h,i} l_m^k \mathrm{d}z \,,\end{aligned} \tag{35b}$$

for all Lagrange interpolating polynomials l_m^k, $m = 1, \ldots, N_p^z$. In Eq. (35), $\hat{\boldsymbol{n}}$ is the outward pointing unit normal, $\partial\Omega_z^k$ are the edges of Ω_z^k, $h_{h,i} = v_{int} c_{h,i} - \sqrt{D_{\mathrm{ax}}} g_{h,i}$ is an approximate solution to h_i, $j_{h,i} = k_{\mathrm{film},i}\left(c_{h,i} - c_{h,p,i}\big|_{r=R_p}\right)$ is an approximate solution to j_i and $c_{h,p,i}$ is an approximate solution to the pore phase concentration $c_{p,i}$ defined later in section 3.3.

As a consequence of the finite dimensional test space $\mathbb{V}_h^z$ being broken, the fluxes $h_{h,i}\big|_{\partial\Omega_z^k}$ and $\sqrt{D_{\mathrm{ax}}} c_{h,i}\big|_{\partial\Omega_z^k}$ are multiply defined on all axial element interfaces (see Fig. 2). To obtain a unique and global solution, these are replaced by the numerical flux functions $h_i^*\big|_{\partial\Omega_z^k}$ and $\sqrt{D_{\mathrm{ax}}} c_i^*\big|_{\partial\Omega_z^k}$, respectively, which depend on both the internal and external axial element edge values. The numerical flux functions are specified later in section 3.2.3.

The following weak form is obtained after replacing the nonunique fluxes in Eq. (35) by uniquely defined numerical fluxes:

$$\begin{aligned}\int_{\Omega_z^k} \frac{\partial c_{h,i}}{\partial t} l_m^k \mathrm{d}z = &\int_{\Omega_z^k} h_{h,i} \frac{\partial l_m^k}{\partial z} \mathrm{d}z - \int_{\partial\Omega_z^k} \hat{\boldsymbol{n}} h_i^* l_m^k \mathrm{d}z \\ &- F_c \frac{3}{R_p} \int_{\Omega_z^k} j_{h,i} l_m^k \mathrm{d}z \,,\end{aligned} \tag{36a}$$

$$\begin{aligned}\int_{\Omega_z^k} g_{h,i} l_m^k \mathrm{d}z = &-\sqrt{D_{\mathrm{ax}}} \int_{\Omega_z^k} c_{h,i} \frac{\partial l_m^k}{\partial z} \mathrm{d}z \\ &+ \sqrt{D_{\mathrm{ax}}} \int_{\partial\Omega_z^k} \hat{\boldsymbol{n}} c_i^* l_m^k \mathrm{d}z \,,\end{aligned} \tag{36b}$$

for all Lagrange interpolating polynomials l_m^k, $m = 1, \ldots, N_p^z$.

It is assumed that the approximate solutions $c_{h,i}$ and $g_{h,i}$ can be represented on the kth element as

$$\begin{bmatrix} c_i(z,t) \\ g_i(z,t) \end{bmatrix} \approx \begin{bmatrix} c_{h,i}(z,t) \\ g_{h,i}(z,t) \end{bmatrix} = \sum_{m=1}^{N_p^z} \begin{bmatrix} c_{h,i}(t)\big|_{z_m^k} \\ g_{h,i}(t)\big|_{z_m^k} \end{bmatrix} l_m(\xi_z^k(z)) \,, \tag{37}$$

where $\left\{z_m^k\right\}_{m=1}^{N_p^z}$ is a set of axial grid nodes in the physical element Ω_z^k. Inserting Eq. (37) into (36) gives a system of ordinary differential equations to recover the local solution on the kth element as,

$$\begin{aligned}\frac{\partial \boldsymbol{c}_{h,i}^k}{\partial t} = &\mathcal{J}_z^k \mathcal{M}^{-1} \mathcal{S}^T \boldsymbol{h}_{h,i}^k - F_c \frac{3}{R_p} \boldsymbol{j}_{h,i}^k \\ &- \mathcal{J}_z^k \mathcal{L} \hat{\boldsymbol{n}} h_i^*\big|_{\partial\Omega_z^k} \,,\end{aligned} \tag{38a}$$

$$\begin{aligned}\boldsymbol{g}_{h,i}^k = &-\sqrt{D_{\mathrm{ax}}} \mathcal{J}_z^k \mathcal{M}^{-1} \mathcal{S}^T \boldsymbol{c}_{h,i}^k \\ &+ \sqrt{D_{\mathrm{ax}}} \mathcal{J}_z^k \mathcal{L} \hat{\boldsymbol{n}} c_i^*\big|_{\partial\Omega_z^k} \,,\end{aligned} \tag{38b}$$

where

$$\boldsymbol{c}_{h,i}^k = \left[c_{h,i}(t)\big|_{z_1^k}, \ldots, c_{h,i}(t)\big|_{z_{N_p^z}^k} \right]^{\mathsf{T}} , \tag{39}$$

is a vector of nodal mobile phase concentrations,

$$\boldsymbol{h}_{h,i}^k = \left[h_{h,i}(t)\big|_{z_1^k}, \ldots, h_{h,i}(t)\big|_{z_{N_p^z}^k} \right]^{\mathsf{T}} , \tag{40}$$

is a vector of nodal mobile phase fluxes,

$$\boldsymbol{j}_{h,i}^k = \left[j_{h,i}(t)\big|_{z_1^k}, \ldots, j_{h,i}(t)\big|_{z_{N_p^z}^k} \right]^{\mathsf{T}} , \tag{41}$$

is a vector of nodal fluxes from the mobile phase into the pore phase, and

$$\boldsymbol{g}_{h,i}^k = \left[g_{h,i}(t)\big|_{z_1^k}, \ldots, g_{h,i}(t)\big|_{z_{N_p^z}^k} \right]^{\mathsf{T}} , \tag{42}$$

is a vector of nodal gradient variables.

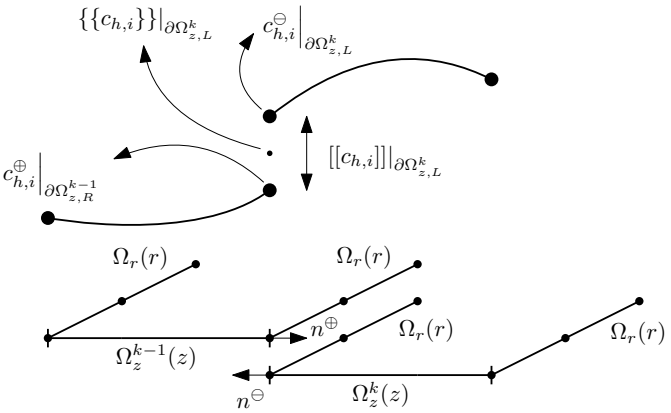

Figure 2: A discontinuous Galerkin interface with notation given for the left interface on the kth axial element with $k = 2, \ldots, N_e - 1$. Note that two radial elements are associated with each interface. $\partial\Omega_{z,L}^k$ is the left interface of the kth element and $\partial\Omega_{z,R}^{k-1}$ is the right interface of the $k-1$th element.

3.2.3. Numerical fluxes

To complete the scheme, suitable numerical fluxes must be specified. The notation

$$\{\{y\}\} = 0.5\left(y^{\ominus} + y^{\oplus}\right), \quad [[y]] = \left(\hat{\boldsymbol{n}}^{\ominus} y^{\ominus} + \hat{\boldsymbol{n}}^{\oplus} y^{\oplus}\right) , \tag{43}$$

is used for the average and jump at boundary interfaces $\partial\Omega_z^k$, respectively (see Fig. 2). In Eq. (43), the superscripts $\ominus$ and $\oplus$ denote the interior and exterior boundary values, respectively.

The numerical flux h_i^* is composed of a convective and a diffusive part, i.e.

$$h_i^* = h_{i,\text{conv}}^* + h_{i,\text{diff}}^* \,, \tag{44}$$

where

$$h_{i,\text{conv}}^* = v_{\text{int}} c_i^* \left(c_{h,i}^{\ominus}, c_{h,i}^{\oplus} \right) \,, \tag{45a}$$

$$h_{i,\text{diff}}^* = -\sqrt{D_{\text{ax}}} g_i^* \left(g_{h,i}^{\ominus}, g_{h,i}^{\oplus} \right) \,. \tag{45b}$$

The convective part of the flux is for the ith component approximated by a Lax-Friedrichs flux

$$h_{i,\text{conv}}^* = v_{\text{int}} \left\{ \{ c_{h,i} \} \right\} + 0.5 v_{\text{int}} \left[[c_{h,i}] \right] \,, \tag{46}$$

which simplifies to an upwind flux due to linearity of the convective flux. For the diffusive flux, an internal penalty flux (Douglas and Dupont, 1976; Douglas et al., 2002) is chosen

$$h_{i,\text{diff}}^* = \sqrt{D_{ax}} \left(\{ \{ g_{h,i} \} \} - \tau \left[[c_{h,i}] \right] \right) \,, \tag{47}$$

where τ is a penalizing constant to control jumps in the solution of $c_{h,i}^k$. It is chosen using the following scaling

$$\tau = \frac{(N^z)^2}{\Delta z^k} \,, \tag{48}$$

where a central flux is obtained by specifying $\tau = 0$.

Finally, the numerical flux $\sqrt{D_{ax}} c_i^*$ is specified for the ith component as the central flux

$$\sqrt{D_{\text{ax}}} c_i^* = \sqrt{D_{\text{ax}}} \left\{ \{ c_{h,i} \} \right\} \,, \tag{49}$$

such that $\boldsymbol{g}_{h,i}^k$ can be eliminated locally in Eq. (38).

3.2.4. Boundary conditions

The boundary conditions are imposed weakly through the numerical fluxes by exploiting a symmetry principle.

The inlet Robin condition Eq. (9) is imposed for the ith component by specifying the external convective flux at the column inlet $z = 0$ as

$$\begin{aligned} v_{\text{int}} \, c_{h,i}^{\oplus}(t) \big|_0 &= 2 v_{\text{int}} c_{\text{inj},i}(t) - v_{\text{int}} \, c_{h,i}^{\ominus}(t) \big|_0 \\ &\Rightarrow v_{\text{int}} \left\{ \{ c_{h,i}(t) \} \right\} \big|_0 = v_{\text{int}} c_{\text{inj},i}(t) \,, \end{aligned} \tag{50}$$

and the external diffusive flux as

$$\begin{aligned} \sqrt{D}_{\text{ax},i} \, g_{h,i}^{\oplus}(t) \big|_0 &= -\sqrt{D}_{\text{ax},i} \, g_{h,i}^{\ominus}(t) \big|_0 \\ &\Rightarrow \sqrt{D}_{\text{ax},i} \left\{ \{ g_{h,i}(t) \} \right\} \big|_0 = 0 \,, \end{aligned} \tag{51}$$

such that the convective-dispersive mobile phase flux equals the inlet flux on average.

The outlet Neumann condition Eq. (11) is implemented for the ith component by defining the external convective flux on the column outlet at $z = L$ as

$$\begin{aligned} v_{\text{int}} \, c_{h,i}^{\oplus}(t) \big|_L &= v_{\text{int}} \, c_{h,i}^{\ominus}(t) \big|_L \\ &\Rightarrow v_{\text{int}} \left\{ \{ c_{h,i}(t) \} \right\} \big|_L = v_{\text{int}} \, c_{h,i}^{\ominus} \big|_L \,, \end{aligned} \tag{52}$$

such that it is unmodified and the external diffusive flux as

$$\begin{aligned} \sqrt{D}_{\text{ax},i} \, g_{h,i}^{\oplus}(t) \big|_L &= -\sqrt{D}_{\text{ax},i} \, g_{h,i}^{\ominus}(t) \big|_L \\ &\Rightarrow \sqrt{D}_{\text{ax},i} \left\{ \{ g_{h,i}(t) \} \right\} \big|_L = 0 \,, \end{aligned} \tag{53}$$

such that it is zero on average.

Since the boundary conditions are imposed through the numerical flux h_i^*, the external fluxes required to compute $\sqrt{D_{\text{ax}}} c_i^*$ on the domain end points are specified such that the solution is unmodified. That gives for the ith component

$$\begin{aligned} &\sqrt{D}_{\text{ax},i} \, c_{h,i}^{\oplus}(t) \big|_0 = \sqrt{D}_{\text{ax},i} \, c_{h,i}^{\ominus} \big|_0 \\ &\quad \Rightarrow \sqrt{D}_{\text{ax},i} \left\{ \{ c_{h,i}(t) \} \right\} \big|_0 = \sqrt{D}_{\text{ax},i} \, c_{h,i}^{\ominus}(t) \big|_0 \,, \end{aligned} \tag{54a}$$

$$\begin{aligned} &\sqrt{D}_{\text{ax},i} \, c_{h,i}^{\oplus} \big|_L = \sqrt{D}_{\text{ax},i} \, c_{h,i}^{\ominus} \big|_L \\ &\quad \Rightarrow \sqrt{D}_{\text{ax},i} \left\{ \{ c_{h,i}(t) \} \right\} \big|_L = \sqrt{D}_{\text{ax},i} \, c_{h,i}^{\ominus}(t) \big|_L \,. \end{aligned} \tag{54b}$$

3.3. Spatial discretization in the radial direction

In this section, the radial differential operators in Eq. (2) are discretized using a discontinuous Galerkin spectral method.

3.3.1. Computational domain

The computational domain Ω_r is composed of a single radial element. The domain Ω_r is mapped to the standard element by an affine mapping

$$\xi_r(r) = \frac{2r}{R_p} - 1 \,, \tag{55}$$

where $\mathcal{J}_r = 2/R_p$ is the Jacobian of the affine mapping.

3.3.2. General formulation

The finite-dimensional weak formulation for the pore phase concentrations takes the following form for the ith component and the kth axial element: Find $c_{h,p,i} \in \mathbb{V}_h^r$ and $q_{h,i} \in \mathbb{V}_h^r$ such that

$$\begin{aligned} &\int_{\Omega_z^k} \int_{\Omega_r} \left(\frac{\partial c_{h,p,i}}{\partial t} + F_p \frac{\partial q_{h,i}}{\partial t} \right) r^2 l_m(r) \mathrm{d}r l_n^k(z) \mathrm{d}z \\ &= -\int_{\Omega_z^k} \int_{\Omega_r} \Bigg(D_{p,i} \frac{\partial c_{h,p,i}}{\partial r} \\ &\quad + D_{\text{s},i} F_p \frac{\partial q_{h,i}}{\partial r} \Bigg) r^2 \frac{\partial l_m}{\partial r} \mathrm{d}r l_n^k(z) \mathrm{d}z \\ &\quad + \int_{\Omega_z^k} \int_{\partial\Omega_r} \hat{\boldsymbol{n}} \Bigg(D_{\text{p},i} \frac{\partial c_{h,p,i}}{\partial r} \\ &\quad + D_{\text{s},i} F_p \frac{\partial q_{h,i}}{\partial r} \Bigg) r^2 l_m(r) \mathrm{d}r l_n^k(z) \mathrm{d}z \,, \end{aligned} \tag{56}$$

for all Lagrange interpolating polynomials $l_m(r)$, $m = 1, \ldots, N_p^r$ and $l_n^k(z)$, $n = 1, \ldots, N_p^z$. Here, $\partial\Omega_r$ are edges of the radial domain Ω_r, $q_{h,i}$ are approximate solutions to q_i,

and the finite dimensional space of test functions $\mathbb{V}_h^r$ consists of Lagrange interpolating polynomials $l_m(r)$ of order at most $N^r = N_p^r - 1$ and $l_n^k(z)$ of order at most N^z, i.e.

$$\mathbb{V}_h^r = \bigoplus_{k=1}^{N_e} \operatorname{span}\left\{l_n \circ \xi_z^k\right\}_{n=1}^{N_p^z} \otimes \operatorname{span}\left\{l_m \circ \xi_r\right\}_{m=1}^{N_p^r} . \tag{57}$$

It is assumed that the approximate solutions $c_{h,p,i}$ and $q_{h,i}$ can be represented on the kth axial element as

$$\begin{aligned}\begin{bmatrix} c_{p,i}(z,r,t) \\ q_{h,i}(z,r,t) \end{bmatrix} &\approx \begin{bmatrix} c_{h,p,i}(z,r,t) \\ q_{h,i}(z,r,t) \end{bmatrix} \\ &= \sum_{n=1}^{N_p^z}\sum_{m=1}^{N_p^r} \begin{bmatrix} c_{h,p,i}(t)\big|_{(z_n^k,r_m)} \\ q_{h,i}(t)\big|_{(z_n^k,r_m)} \end{bmatrix} l_n\left(\xi_z^k(z)\right) l_m\left(\xi_r(r)\right) ,\end{aligned} \tag{58}$$

where $\{r_m\}_{m=1}^{N_p^r}$ is a set of radial grid nodes in the physical element Ω_r. Inserting Eq. (58) and the boundary conditions (12) and (13) into (56) gives the following system of ordinary differential equations

$$\begin{aligned}\frac{\partial \boldsymbol{c}_{h,p,i}^{k,n}}{\partial t} &= -\mathcal{J}_r^2\left(\mathcal{M}^{(0,2)}\right)^{-1}\mathcal{A}^{(0,2)}\left(D_{\mathrm{p},i}\boldsymbol{c}_{h,p,i}^{k,n} + D_{\mathrm{s},i}F_p\boldsymbol{q}_{h,i}^{k,n}\right) \\ &\quad + \mathcal{J}_r^3\mathcal{L}^{(0,2)}\begin{bmatrix} 0 \\ \left(j_i/\varepsilon_p\right)R_p^2 \end{bmatrix},\end{aligned} \tag{59}$$

for all axial grid nodes z_n^k, $n = 1,\ldots,N_p^z$. Here,

$$\boldsymbol{c}_{h,p,i}^{k,n} = \left[c_{h,p,i}(t)\big|_{z_n^k,r_1}, \ldots, c_{h,p,i}(t)\big|_{z_n^k,r_{N_p^r}} \right] , \tag{60}$$

is a vector of nodal pore phase concentrations, and

$$\boldsymbol{q}_{h,i}^{k,n} = \left[q_{h,i}(t)\big|_{z_n^k,r_1}, \ldots, q_{h,i}(t)\big|_{z_n^k,r_{N_p^r}} \right] , \tag{61}$$

is a vector of nodal stationary phase concentrations.

3.4. Discretization of the stationary phase concentrations

The finite-dimensional weak formulation for the stationary phase concentrations takes the following form for the ith component and the kth axial element: Find $c_{h,p,i} \in \mathbb{V}_h^r$ and $q_{h,i} \in \mathbb{V}_h^r$ such that

$$\int_{\Omega_z^k}\int_{\Omega_r} q_{h,i}l_m(r)\mathrm{d}r l_n^k(z)\mathrm{d}z = \int_{\Omega_z^k}\int_{\Omega_r} \omega_{h,i}l_m(r)\mathrm{d}r l_n(z)\mathrm{d}z , \tag{62}$$

for all Lagrange interpolating polynomials $l_m(r)$, $m = 1,\ldots,N_p^r$ and $l_n^k(z)$, $n = 1,\ldots,N_p^z$. Here,

$$\omega_{h,i} = c_{h,p,i}A_{h,i}\left(1 - \sum_{j=1}^{N_c}\frac{q_{h,j}}{q_{\max,j}}\right)^{\nu_i} , \tag{63}$$

are approximations to the isotherm functions ω_i and $A_{h,i} = K_{\mathrm{eq},i}\left(\Lambda/c_{h,p,0}\right)^{\nu_i}$ are approximations to the initial isotherm slopes A_i.

It is assumed that the approximate isotherm functions $\omega_{h,i}$ can be represented on the kth axial element as

$$\begin{aligned}\omega_i(z,r,t) &\approx \omega_{h,i}(z,r,t) \\ &= \sum_{n=1}^{N_p^z}\sum_{m=1}^{N_p^r} \omega_{h,i}(t)\big|_{z_n^k,r_m} l_n\left(\xi_z^k(z)\right) l_m\left(\xi_r(r)\right) .\end{aligned} \tag{64}$$

Note that such an interpolation can introduce aliasing errors on coarse grids since ω_i is a non-linear function. These errors can be reduced without increasing the discrete problem size by using e.g. spectral filtering or over-integration techniques at increased computational cost (Gassner and Beck, 2013; Engsig-Karup et al., 2016). In this work, it is accepted that aliasing errors might occur on coarse grids and they are removed by increasing the grid resolution if necessary.

Inserting Eq. (64) into (62) gives a set of algebraic constraints

$$\boldsymbol{q}_{h,i}^{k,n} = \boldsymbol{\omega}_{h,i}^{k,n} , \tag{65}$$

for all axial grid nodes z_n^k, $n = 1,\ldots,N_p^z$. In Eq. (65),

$$\boldsymbol{\omega}_{h,i}^{k,n} = \left[\omega_{h,i}(t)\big|_{z_n^k,r_1}, \ldots, \omega_{h,i}(t)\big|_{z_n^k,r_{N_p^r}} \right] , \tag{66}$$

is a vector of nodal isotherm functions.

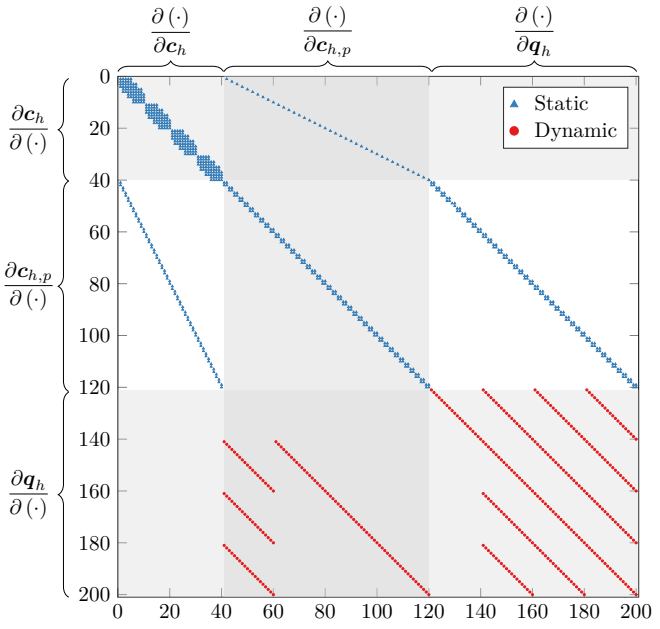

Figure 3: Sparsity pattern for the matrix $d\boldsymbol{F}/d\boldsymbol{u}$ in Eq. (71) for a four component system ($N_c = 4$, $N_e = 5$, $N^z = 1$, $N^r = 1$). The blue triangles and red circles represent static and dynamic dependencies, respectively.

3.5. Temporal discretization

In this section, the time-integration of the system of differential algebraic equations obtained after spatial discretization is described.

3.5.1. The residual formulation

The semi-discrete system of differential algebraic equations is advanced in time in fully implicit form:

$$F(t, \boldsymbol{u}, \boldsymbol{u}') = 0, \quad \boldsymbol{u}|_{t=0} = \boldsymbol{u}_0, \quad \boldsymbol{u}'\big|_{t=0} = \boldsymbol{u}'_0\,, \tag{67}$$

where $\boldsymbol{u} = \left[\boldsymbol{c}_h, \boldsymbol{c}_{p,h}, \boldsymbol{q}_h\right]^\intercal \in \mathcal{R}^{N_c N_e N_p^z + 2N_c N_e N_p^z N_p^r}$ is the state vector with $\boldsymbol{c}_h \in \mathcal{R}^{N_c N_e N_p^z}$, $\boldsymbol{c}_{h,p} \in \mathcal{R}^{N_c N_e N_p^z N_p^r}$ and $\boldsymbol{q}_h \in \mathcal{R}^{N_c N_e N_p^z N_p^r}$, $\boldsymbol{u}_0$ contains the initial conditions, and $\boldsymbol{u}'$ contains the time derivative of the state vector.

Eq. (67) is advanced in time using the implicit differential-algebraic (IDA) solver from the suite of nonlinear and differential-algebraic equation solvers (SUNDIALS) (Hindmarsh et al., 2005). While implicit-explicit operator splitting is useful in special cases (Meyer et al., 2018a), IDA uses a more generally applicable variable-order variable-coefficient backward differentiation formula in fixed-leading-form (Brenan et al., 1996) to represent the temporal operator, i.e.

$$\boldsymbol{u}'_l = \Delta t_l^{-1} \sum_{n=0}^{N_q} \psi_{l,n} \boldsymbol{u}_{l-n}\,, \tag{68}$$

where $\boldsymbol{u}'_l = \boldsymbol{u}'|_{t_l}$ and $\boldsymbol{u}_{l-n} = \boldsymbol{u}|_{t_l - n\Delta t}$, l is the current time step index, Δt_l is the current time step length, $N_q \in [1, 5]$ is the order of the method and $\psi_{l,n}$ are coefficients uniquely determined by the order and the history of the time step sizes. IDA uses an internal strategy to adaptively change the time step length, the order of the method, and the corresponding coefficients. Combining Eqs. (67) and (68) results in the following nonlinear algebraic system to be solved at each time step:

$$G(\boldsymbol{u}_l) = F\left(t_l, \boldsymbol{u}_l, \Delta t_l^{-1} \sum_{n=0}^{N_q} \psi_{l,n} \boldsymbol{u}_{l-n}\right) = 0\,. \tag{69}$$

Eq. (69) is solved using modified Newton iterations. In each modified Newton iteration, a linear system of the following form is solved:

$$\boldsymbol{J}[\boldsymbol{u}_l^{p+1} - \boldsymbol{u}_l^p] = -G(\boldsymbol{u}_l^p)\,, \tag{70}$$

where p is the current Newton iteration. In Eq. (70), $\boldsymbol{J}$ is an approximation to the system Jacobian

$$\boldsymbol{J} = \frac{\mathrm{d}\boldsymbol{G}}{\mathrm{d}\boldsymbol{u}} = \frac{\mathrm{d}\boldsymbol{F}}{\mathrm{d}\boldsymbol{u}} + \psi \frac{\mathrm{d}\boldsymbol{F}}{\mathrm{d}\boldsymbol{u}'}\,, \tag{71}$$

where $\psi = \psi_{l,0}/\Delta t_l$. IDA uses an internal strategy to adaptively update the Jacobian when required.

3.5.2. Computing the Jacobian

The Jacobian Eq. (71) is derived by hand and computed analytically. Fig. 3 shows a sparsity pattern $\boldsymbol{S}$ of the Jacobian $d\boldsymbol{F}/d\boldsymbol{u}$ for a four component system ($N_e = 4$, $N^z = 1$, $N^r = 1$). The sparsity pattern is defined such that

$$\boldsymbol{S}_{nm} = \begin{cases} 1, & \text{if } (d\boldsymbol{F}/d\boldsymbol{u})_{nm} \neq 0, \\ 0, & \text{otherwise}\,. \end{cases} \tag{72}$$

The discontinuous Galerkin spectral element method is a linear discretization method. Therefore, the dependencies on Eqs. (38) and (59) result in static entries in the Jacobian. These entries are pre-computed and reused in every Jacobian update. The entries due to the non-linear steric-mass-action isotherm Eq. (65) are dynamically changing and have to be re-computed each time the Jacobian is updated.

The Jacobian $d\boldsymbol{F}/d\boldsymbol{u}'$ is fully static and is pre-computed and reused in every Jacobian update.

3.5.3. Consistent initial conditions

The time derivative of the initial state $\boldsymbol{u}'_0$ must be consistent with $\boldsymbol{u}_0$ for the chosen inlet conditions $c_{\mathrm{inj},i}\big|_{t=0}$, $\forall i = 0, \ldots, N_c$.

Choosing the initial states $\boldsymbol{u}_0$ as described in section 2.4 ensures that the algebraic constraints are satisfied. Using these initial states, a consistent state derivative $\boldsymbol{u}'$ can be computed from Eq. (67) by evaluating it at the initial time point $t = 0$.

3.6. Implementation details

ChromaTech has been implemented in C++ for performance. To enable cross-platform compatibility, the CMake build system (CMake, 2019) is used. It allows the development of build scripts, that simplify the configuration and installation procedure. The code is compiled with the LLVM 9.0.0 compiler using the Clang front-end (LLVM, 2019). IDA 4.1 is built using sequential operations, since the overhead of using a parallel implementation is too large for the relatively small systems solved here. The generic SUNDIALS modules NVECTOR, SUNMatrix and SUNLinearSolve have been overridden using custom implementations based on Eigen 3.3.7 (Gaël et al., 2010), a C++ template library for linear algebra, matrices and vectors. Sparse matrices are stored in compressed column major order, and dense matrices in column-major order. Linear systems are solved using Eigen's sparse supernodal LU factorization, a general purpose library for the solution of large, sparse, nonsymmetric systems of linear equations. Other linear solvers including a direct shared-memory parallelized supernode-based LU-factorization (Demmel et al., 1999a,b) have also been tested. However, the parallelization of the decomposition method was not beneficial for the relatively small linear systems solved in this work (results are not shown).

3.7. Differences in ChromaTech compared to CADET

Both ChromaTech and CADET are based on a method of lines approach. CADET uses a second (low) order accurate finite volume method for spatial discretization both in the axial and radial directions leading to a relatively large state vector $\boldsymbol{u}$. In comparison, the state vector $\boldsymbol{u}$ obtained by ChromaTech has a much smaller dimension due to its spectral engine.

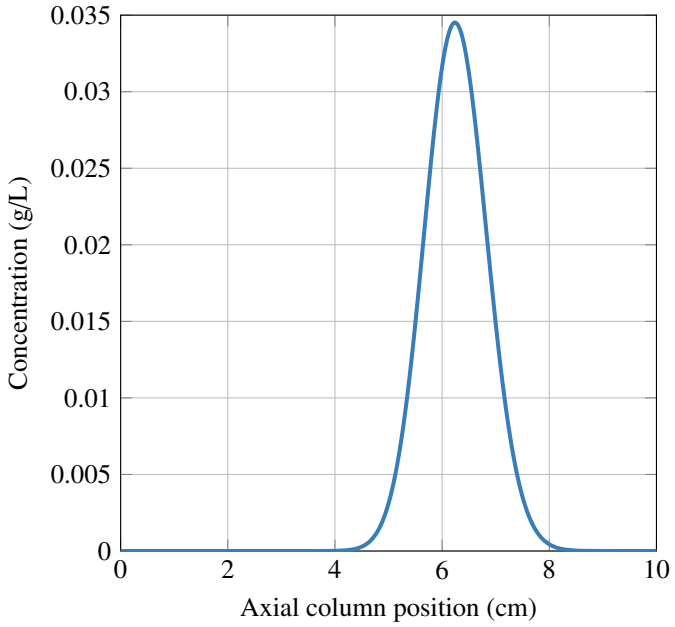

Figure 4: Mobile phase concentrations shown over axial column positions at the final simulation time t_f = 250 min for the validation case (section 5.1). The model parameters taken from Qamar et al. (2014) are given in Table 1.

ChromaTech advances the semi-discrete scheme in time using IDA which is similar to CADET. ChromaTech uses a modified Newton's method to solve the nonlinear system Eq. (69). That is, the Jacobian Eq. (71) is formed and factorized adaptively and not at every iteration using IDA's internal strategy as mentioned previously in section 3.5.1. In comparison, CADET uses a full Newton's method where the Jacobian is formed and decomposed in every Newton iteration. Forming the Jacobian matrix in every iteration speeds up the nonlinear solution procedure such that less Newton iterations are required to meet the tolerance. However, the Jacobian matrix has to be formed and factorized often which can be costly. The impact of this trade-off on computational efficiency is problem dependent.

Due to the different dimensions of the state vector $\boldsymbol{u}$, different strategies for solving the linear system Eq. (70) are employed. ChromaTech solves the linear system Eq. (70) using a direct method, since its dimension is small. In comparison, CADET splits the Jacobian Eq. (71) into smaller subsystems by domain decomposition. Here, additional algebraic constraints are introduced to link the subsystems. Then, the linear subsystems can be solved independently in parallel (details are given by von Lieres and Andersson (2010)). Due to the efficiency of this strategy for solving linear systems, it is beneficial to use a full Newton's method in CADET.

4. Analytical solution technique

Analytical solutions have been derived for single-component chromatography models including pores, linear adsorption and no axial dispersion (Rosen model) but lacking a closed-form solution (Rodrigues, 1984). However, there is no closed-form analytical solution known to us in the time-domain for the single component general rate model presented in this work. Therefore, an analytical solution in the Laplace domain is used (Qamar et al., 2014; Miyabe, 2014; Leweke and von Lieres, 2016). The mobile phase concentration c in the Laplace domain $\bar{c}$ is

$$\begin{aligned}\bar{c}(s,z) = \bar{c}_{\text{in}}(s)\frac{\beta_1(s)}{\bar{c}_{\text{in}}(s)}\exp\left(\lambda_1(s)z\right) \\ + \bar{c}_{\text{in}}(s)\frac{\beta_2(s)}{\bar{c}_{\text{in}}(s)}\exp\left(\lambda_2(s)z\right)\ ,\end{aligned} \tag{73}$$

where s is the complex Laplace frequency, and $\bar{c}_{in}(s)$ is an inlet function in the Laplace domain. Moreover, the functions λ_1, λ_2, β_1 and β_2 are given by e.g. Leweke and von Lieres (2016).

The open source software package CADET-semi-analytic (Leweke and von Lieres, 2016) is used to invert Eq. (73) numerically. It supports arbitrary precision arithmetics to minimize the impact of round-off errors and gives solutions that satisfy a proven error bound at the axial column end position, $z = L$ (see Leweke and von Lieres (2016) for details). Note that CADET-semi-analytic cannot be used to obtain accurate solutions at and in the neighbourhood of the column inlet position $z = 0$ since the solution has a pole here.

5. Numerical case studies

In this section, three cases are considered to validate and test the performance of ChromaTech.

All computations are conducted on a MacBook Pro (Early 2015) equipped with a dual core 2.7 GHz Intel Core i5 processor, 8 GB 1867 MHz DDR3 RAM and a 64-bit OS X operating system.

CADET 4.0.0 is used as a performance benchmark. It is build for OS X using a GNU 9.1 compiler with dependencies: IDA 3.1.2, Intel(R)'s Math Kernel Library version 2019.1.3, and Intel(R)'s Threading Building Blocks 2019.0.

5.1. Case 1: Validation of ChromaTech

The purpose of this case is to validate that ChromaTech's engine is correctly implemented. Here, a simple case is studied where a one-component feed mixture is injected at the column inlet under linear adsorption conditions.

The model problem is taken from Qamar et al. (2014) and modified such that it is easier to demonstrate correct implementation of ChromaTech. The detailed simulation parameters are given in Table 1. The column length has been modified from 1.7 cm to 10 cm while maintaining the same dispersion coefficient. For computational reasons, it

Table 1: Simulation parameters taken from Qamar et al. (2014). They are used in the validation case with a single component (section 5.1)

Parameters	Symbol	Values	Unit
Components	N_c	1	-
Column porosity	ε_c	0.4	-
Particle porosity	ε_p	0.333	-
Particle radius	R_p	0.004	cm
Film diffusion coefficient	$k_{\text{film},1}$	0.01	cm min^{-1}
Interstitial velocity	v_{int}	0.1	cm min^{-1}
Axial dispersion coefficient	D_{ax}	0.002	$\text{cm}^2\,\text{min}^{-1}$
Pore diffusion coefficient	$D_{\text{p},1}$	$6.3845 \cdot 10^{-5}$	$\text{cm}^2\,\text{min}^{-1}$
Surface diffusion coefficient	$D_{\text{s},1}$	0	$\text{cm}^2\,\text{min}^{-1}$
Initial isotherm slope	A_1	2.5	-
Feed concentration	$c_{\text{f},1}$	1	g l^{-1}

Table 2: Mobile phase errors measured in the continuous $L^1_{\Omega_z}$- ($\text{g l}^{-1}\,\text{cm}$), $L^2_{\Omega_z}$- ($\text{g l}^{-1}\,\sqrt{\text{cm}}$), and $L^\infty_{\Omega_z}$-norms (g l^{-1}) and corresponding convergence rates for the validation case (see fully resolved simulation in Fig. 4). The polynomial order in the radial direction N^r_p and the time integration tolerances was chosen carefully not to affect the accuracy of the simulations.

N^z	N_e	$L^1_{\Omega_z}$-error	$L^2_{\Omega_z}$-error	$\text{L}^\infty_{\Omega_z}$-error	$L^1_{\Omega_z}$-order	$L^2_{\Omega_z}$-order	$L^\infty_{\Omega_z}$-order	Theor.
1	128	1.24E−04	1.30E−04	8.54E−05	-	-	-	2
	256	2.74E−05	2.76E−05	1.83E−05	2.18	2.23	2.22	
	512	6.34E−06	6.28E−06	4.18E−06	2.11	2.14	2.13	
	1024	1.52E−06	1.49E−06	9.94E−07	2.06	2.07	2.07	
2	64	8.64E−06	5.10E−06	3.64E−06	-	-	-	3
	128	9.27E−07	5.74E−07	4.06E−07	3.22	3.15	3.17	
	256	1.13E−07	6.81E−08	4.81E−08	3.03	3.07	3.08	
	512	1.47E−08	8.20E−09	5.89E−09	2.95	3.05	3.03	
3	64	4.35E−07	2.59E−07	1.79E−07	-	-	-	4
	128	2.45E−08	1.79E−08	1.24E−08	4.15	3.86	3.86	
	256	1.43E−09	1.14E−09	7.89E−10	4.10	3.97	3.97	
	512	8.85E−11	7.08E−11	4.91E−11	4.01	4.01	4.01	
		-						
4	32	2.82E−07	1.50E−07	1.08E−07	-	-	-	5
	64	7.87E−09	4.18E−09	2.98E−09	5.16	5.17	5.18	
	128	2.64E−10	1.24E−10	8.86E−11	4.9	5.08	5.07	
	256	9.21E−12	3.79E−12	2.74E−12	4.84	5.03	5.02	
		-						

is beneficial to use a long column, since convergence rates are to be determined over the spatial domain. To obtain a smooth solution profile, a slow interstitial velocity of $v_{\text{int}} = 0.1$ is specified. Due to smoothness of the solution profile, convergence rates from numerical experiments can be expected to be in agreement with theoretical ones, providing a condition to verify that the code is working as expected. The feed mixture is injected for 2 min into an empty column, and the final simulation time is specified as $t_f = 250$ min. The injection profile is assumed to be rectangular. A high-precision simulation is shown in Fig. 4 obtained using ChromaTech ($N^z_e = 20$, $N^z = 10$, $N^r = 15$).

A reference solution $\boldsymbol{u}_{\text{ref}}$ is computed using CADET-semi-analytic. To avoid round-off errors in the computations, 100 decimal digit precision is specified. Moreover, a proven error in the sup-Norm of $E_{\text{des}} = 1{\times}10^{-40}$ is specified. This error bound is proven only at the column end position $z = L$. As previously mentioned in section 4, CADET-semi-analytic is unable to produce an accurate solution at and in the neighbourhood of the column inlet position $z = 0$. Thus, an accurate reference can be obtained only in part of the domain $\Omega_z = [0, 10]$, i.e. in $[3, 10]$. The validation case has been designed such that the concentration $c_1(z)$ is equal to zero in double precision for $z \in [0, 3]$ at the final simulation time $t_f = 250$ min (see fully resolved simulation in Fig. 4). Thus, the reference solution $c_{1,\text{ref}}(z)$ is set equal to zero for $z \in [0, 3]$.

In the following, simulated mobile phase concentrations

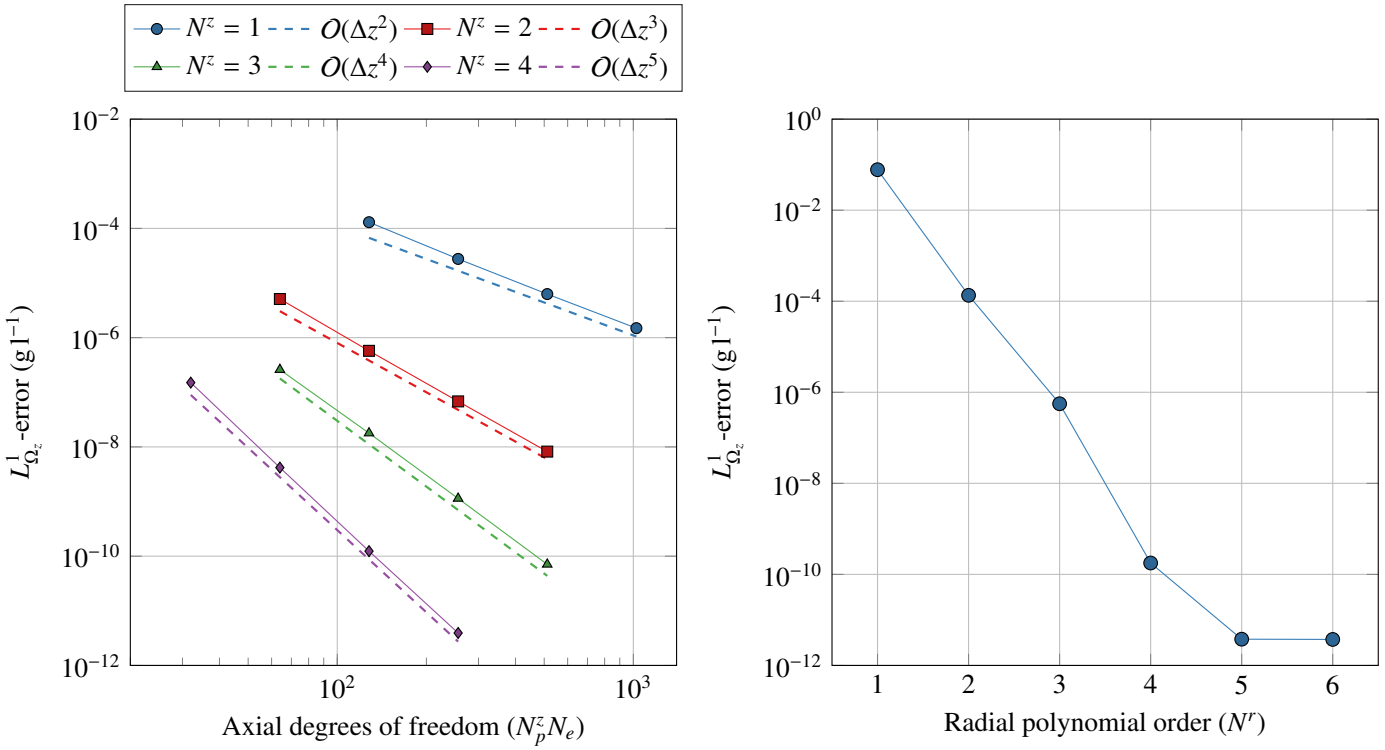

(a) Axial convergence

(b) Radial convergence

Figure 5: $L^1_{\Omega_z}$-errors due to (a) axial and (b) radial approximation errors of the mobile phase concentration as a function of (a) axial degrees-of-freedom and (b) radial polynomial order used within each radial single-element domain for the validation case (see Fig. 4). Results are shown in (a) logarithmic and (b) base-10 scale with data given in Table 2.

are compared with the reference over the spatial domain Ω_z. Convergence rates are computed numerically by comparing simulations obtained using different grid resolutions with the reference.

The approximation errors due to the axial operators are investigated first. Polynomials of order $N^r = 10$ are used to discretize the radial operators on all axial grid nodes, such that radial approximation errors do not affect the accuracy of the simulations. Moreover, the relative and absolute tolerance of IDA are chosen as 1×10^{-12} and 1×10^{-14}, respectively, to ensure negligible errors due to the time discretization. Then, the discrepancies between the simulations and the reference solution are expected to be caused by axial approximation errors only. That is until other sources of errors start to influence the results, e.g. round-off errors due to double precision arithmetics.

Fig. 5(a) shows comparisons of simulations with the reference measured in the continuous $L^1_{\Omega_z}$-norm for different axial grid resolutions. The axial grid resolution is increased by the number of elements N_e^z for fixed polynomial orders $N^z \in \{1, \ldots, 4\}$. The resulting $L^1_{\Omega_z}$-errors are displayed against the grid resolution on a logarithmic plot. The slopes (convergence orders) of each of the linear segments in Fig. 5(a) are listed in Table 2. Additionally, it lists the continuous $L^2_{\Omega_z}$-, and $L^\infty_{\Omega_z}$-errors. In these numerical experiments, the $L^1_{\Omega_z}-$ and $L^2_{\Omega_z}$-errors are evaluated using the mass matrix Eq. (24a) based on a sufficient number of Legendre-Gauss-Lobatto quadrature nodes to ensure negligible integration errors. From Fig. 5(a) and Table 2, it is evident that the convergence rates are of order N^z+1. This is in agreement with theoretical expected ones, validating that the procedure for spatial discretization in the axial direction is correctly implemented. Moreover, it demonstrates, that IDA, CADET-semi-analytic, and the radial discretization procedure are working as expected.

The properties of the radial discretization procedure are investigated next. Here, 20 axial elements are used with 10th order polynomials in each axial element ($N_e^z = 20$, $N^z = 10$), to ensure that errors due to discretization of the axial operators are negligible. Fig. 5(b) shows the $L^1_{\Omega_z}$-errors evaluated for different radial grid resolutions in a semi-logarithmic plot. The results demonstrate, that a rapid exponential convergence rate is obtained as the polynomial order is increased, i.e. spectral convergence is achieved in each radial single-element associated with the axial grid nodes.

5.2. Case 2: Performance benchmark using low load volume

Having successfully tested that ChromaTech's spectral engine is correctly implemented, a less simple problem is considered. The purpose of this case is to test the performance of ChromaTech by benchmarking against CADET.

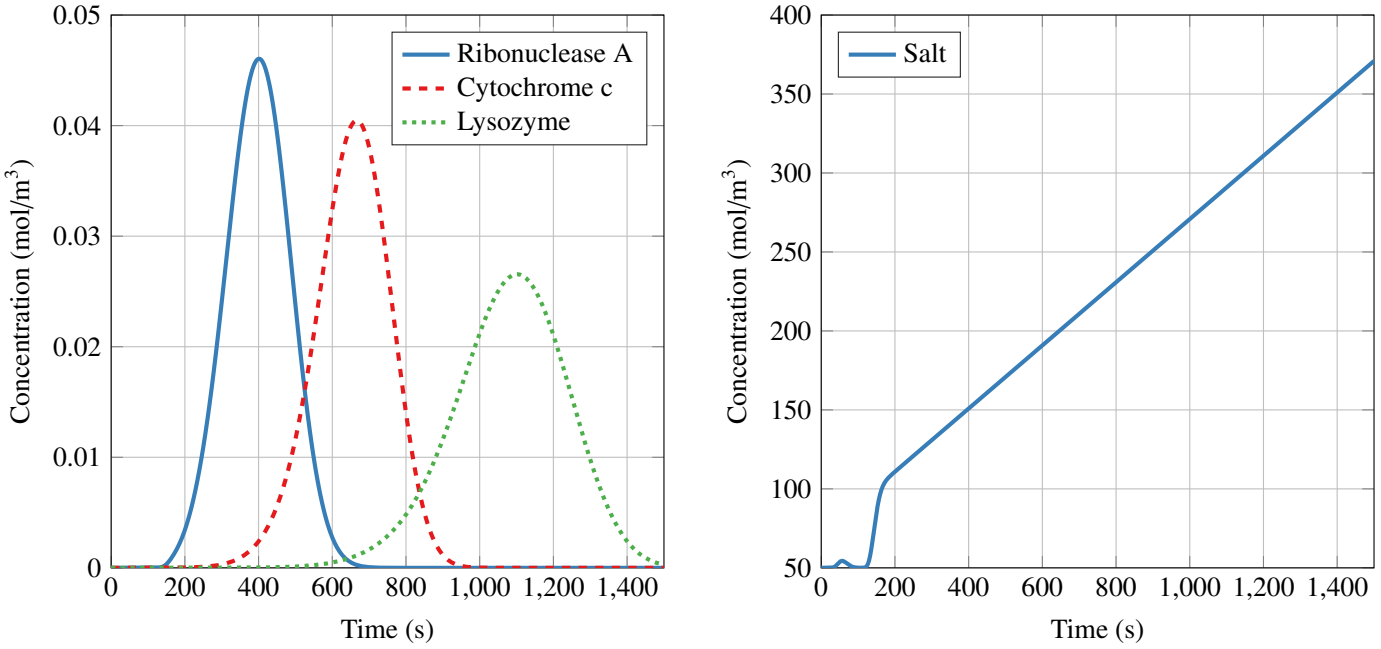

(a) Protein profiles

(b) Salt profile

Figure 6: Mobile phase concentrations at the column outlet of (a) proteins and (b) salt as a function of time (chromatograms) for the performance benchmark using low load volume (section 5.2). The model parameters taken from Püttmann et al. (2013) are given in Table 3.

Table 3: Simulation parameters taken from Püttmann et al. (2013) that are used in the performance benchmark with lysozyme, cytochrome c and ribonuclease A (section 5.2).

Parameters	Symbol	Values	Unit
Components	N_c	4	-
Column length	L	1.4	cm
Particle radius	R_p	0.0045	cm
Column porosity	ε_c	0.37	-
Particle porosity	ε_p	0.75	-
Film diffusion coefficients	$\boldsymbol{k}_{\text{film}}$	$[6.9, 6.9, 6.9, 6.9]^\intercal \cdot 10^{-6}$	$\mathrm{m\,s^{-1}}$
Interstitial velocity	v_{int}	$5.75 \cdot 10^{-4}$	$\mathrm{m\,s^{-1}}$
Axial dispersion coefficients	D_{ax}	$5.75 \cdot 10^{-8}$	$\mathrm{m^2\,s^{-1}}$
Initial salt concentration	$c_{0,\text{init}}$	50	$\mathrm{mol\,m^{-3}}$
Injection concentration	$\boldsymbol{c}_{\text{f}}$	$[-, 1, 1, 1]^\intercal$	$\mathrm{mol\,m^{-3}}$
Injection time	t_{inj}	10	s
Pore diffusion coefficients	$\boldsymbol{D}_{\text{p}}$	$[70, 6.07, 6.07, 6.07]^\intercal \cdot 10^{-11}$	$\mathrm{m^2\,s^{-1}}$
Surface diffusion coefficients	$\boldsymbol{D}_{\text{s}}$	$[0, 0, 0, 0]^\intercal$	$\mathrm{m^2\,s^{-1}}$
Ionic capacity	Λ	1200	$\mathrm{mol\,m^{-3}}$
Thermodynamic equilibrium constants	$\boldsymbol{K}_{\text{eq}}$	$[-, 7.7, 35.5, 1.59]^\intercal \cdot 10^{-3}$	-
Characteristic charges	$\boldsymbol{\nu}$	$[-, 3.7, 4.7, 5.29]^\intercal$	-
Shielding factors	$\boldsymbol{\sigma}$	$[-, 10, 11.83, 10.6]^\intercal$	-

The problem considered is taken from Püttmann et al. (2013). The goal is to separate a three-component protein feed mixture consisting of lysozyme, cytochrome c, and ribonuclease A. A chromatography column packed with a sulphopropyl Sepharose fast flow strong cation exchange resin is used for the separation. The steric-mass-action isotherm is used to describe the non-linear adsorption process. The detailed model parameters are listed in Table 3. Here, it is assumed that surface diffusion is negligible, i.e. $D_{s,i} = 0$, $\forall i = 0, \ldots, N_c$. Note that the injection time t_{inj} is only 10 s leading to linear adsorption dynamics.

The column is initially equilibrated with running salt buffer with an initial salt concentration $c_{0,\text{init}}$ equal to 50 $\mathrm{mol\,m^{-3}}$. The three proteins are loaded onto the column for 10 s, each with a concentration of 1 $\mathrm{mol\,m^{-3}}$, at a constant salt concentration of 50 $\mathrm{mol\,m^{-3}}$. It is assumed that the

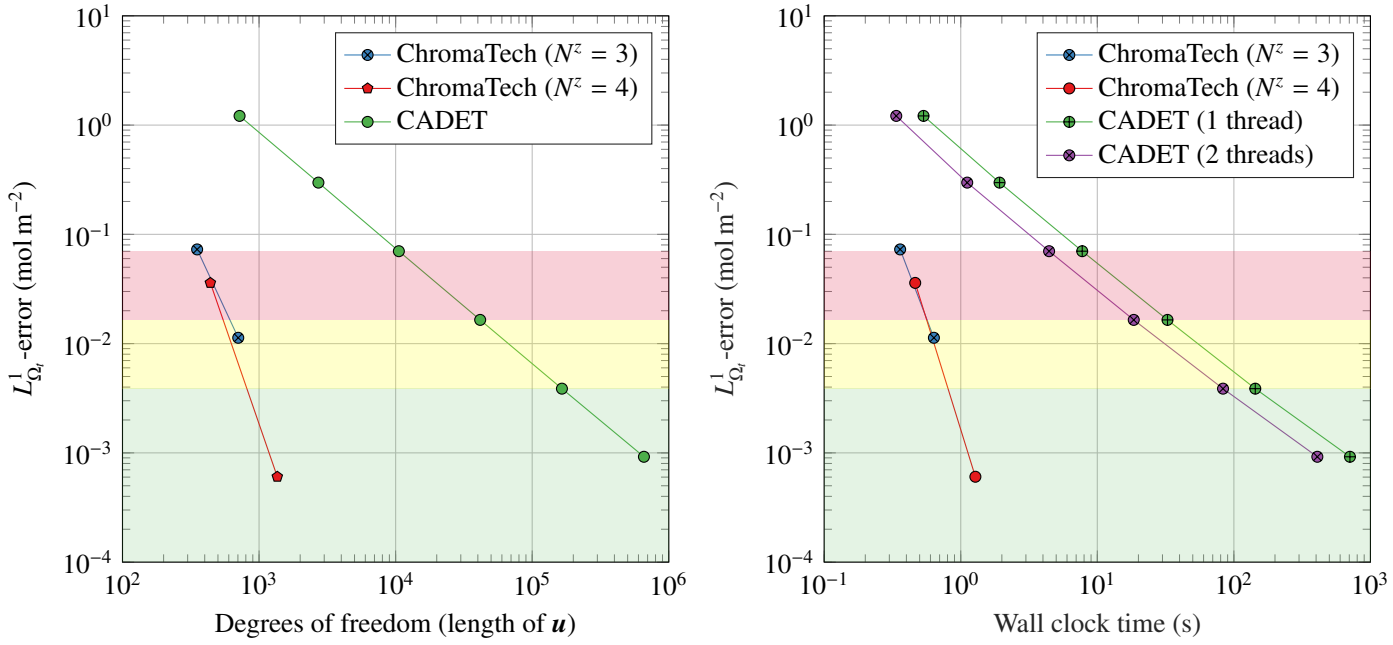

(a) Approximation error against discrete problem size

(b) Approximation error against compute time

Figure 7: The $L^1_{\Omega_t}$-error against computational work in (a) discrete problem size and (b) computational cost measured in wall clock time for the performance benchmark using low load volume (section 5.2). The results are shown in logarithmic scale.

Table 4: Discrete problem size required to obtain low-, engineering- and high-precision simulations with ChromaTech and CADET for the performance benchmark using low load volume (section 5.2). The data is the length of the state-vector $\boldsymbol{u}$ and is visualized in Fig. 7.

Precision	ChromaTech	CADET	Reduction
Low	352	10560	×30
Engineering	704	41600	×59
High	1360	165120	×121

Table 5: Computational cost required to obtain low-, engineering- and high-precision simulations with ChromaTech and CADET for the performance benchmark using low load volume (section 5.2) on a single CPU thread. The data is wall clock times (s) and is visualized in Fig. 7.

Precision	ChromaTech	CADET	speed-up
Low	0.36	7.76	×21
Engineering	0.64	32.66	×51
High	1.28	143.46	×111

injection profile is rectangular. The column is then washed for 80 s using the same inlet buffer, but without proteins in the feed. Finally, the bound proteins are eluted using a linear salt gradient from 90 s to 1500 s starting at 100 mol m^{-3} with a slope of 0.2 m^3 mol^{-1}.

Since no analytical solutions are available for non-linear chromatography models, a high-precision reference solution $\boldsymbol{u}_{\text{ref}}$ has to be relied on for comparisons. The reference solution is computed using ChromaTech (N^z_e = 20, N^z = 10, N^r = 20). Fig. 6(a) and (b) shows high-precision chromatograms for proteins and salt, respectively.

In the following, mobile phase concentrations at the column outlet are compared with the reference over the time domain $\Omega_t = [0, t_f]$. The approximation errors are measured in the continuous $L^1_{\Omega_t}$-norm and are computed using Simpson's rule with 1500 equidistant time points for each component to ensure negligible integration errors. The relative and absolute time integration tolerances are specified as 1×10^{-6} and 1×10^{-8}, respectively, for both ChromaTech and CADET. These tolerances are sufficient for engineering purposes. Then, the quality of the simulations can be controlled by modifying the spatial discretization parameters only.

The quality of the simulations are classified in three categories: low-precision, engineering-precision, and high-precision. Here, a simulation quality of low-precision and engineering-precision indicates that the simulation is visually distinguishable and indistinguishable from the reference solution, respectively. A high-precision simulation quality indicates that the spatial approximation errors approaches a similar magnitude as the temporal errors for the chosen relative and absolute time integration tolerances, although the spatial approximation errors are still larger at this quality level. It can be beneficial to use low-precision simulations during initial studies with the model to reduce labour-time by performing rapid simulations. However, if low-accuracy simulations are used e.g. for model calibration, the model parameters cannot be trusted since they will be lumped with numerical dispersion. Instead, a sim-

Table 6: Simulation parameters taken from von Lieres and Andersson (2010) that are used in the performance benchmark with native and Cy5-labeled lysozyme (section 5.3).

Parameters	Symbol	Values	Unit
Components	N_c	3	-
Column length	L	1.3	m
Particle radius	R_p	$4.5 \cdot 10^{-5}$	m
Column porosity	ε_c	0.70	-
Particle porosity	ε_p	0.60	-
Film diffusion coefficients	$\boldsymbol{k}_{\text{film}}$	$[10^{-5}, 10^{-5}, 10^{-5}]^\intercal \cdot 10^{-6}$	$\mathrm{m\,s^{-1}}$
Interstitial velocity	v_{int}	0.003	$\mathrm{m\,s^{-1}}$
Axial dispersion coefficients	D_{ax}	0.001	$\mathrm{m^2\,s^{-1}}$
Initial salt concentration	$c_{0,\text{init}}$	94.2	$\mathrm{mol\,m^{-3}}$
Injection concentration	$\boldsymbol{c}_{\text{f}}$	$[-, 0.143, 0.00143]^\intercal$	$\mathrm{mol\,m^{-3}}$
Injection time	t_{inj}	5000	s
Pore diffusion coefficients	$\boldsymbol{D}_{\text{p}}$	$[70, 4.0, 4.0]^\intercal \cdot 10^{-11}$	$\mathrm{m^2\,s^{-1}}$
Surface diffusion coefficients	$\boldsymbol{D}_{\text{s}}$	$[0, 0, 0, 0]^\intercal$	$\mathrm{m^2\,s^{-1}}$
Ionic capacity	Λ	1200	$\mathrm{mol\,m^{-3}}$
Thermodynamic equilibrium constants	$\boldsymbol{K}_{\text{eq}}$	$[-, 0.0355, 0.0611]^\intercal \cdot 10^{-3}$	-
Characteristic charges	$\boldsymbol{\nu}$	$[-, 4.7, 3.93]^\intercal$	-
Shielding factors	$\boldsymbol{\sigma}$	$[-, 11.83, 11.83]^\intercal$	-

Table 7: Discrete problem size required to obtain low-, engineering- and high-precision simulations with ChromaTech and CADET for the performance benchmark using high load volume (section 5.3). The data is the length of the state-vector $\boldsymbol{u}$ and is visualized in Fig. 10.

Precision	ChromaTech	CADET	Reduction
Low	810	33024	×41
Engineering	2064	131584	×64
High	2580	525312	×204

Table 8: Computational cost required to obtain low-, engineering- and high-precision simulations with ChromaTech and CADET for the performance benchmark using high load volume (section 5.3) on a single CPU thread. The data is wall clock times (s) and is visualized in Fig. 10.

Precision	ChromaTech	CADET	speed-up
Low	1.52	34.49	×23
Engineering	4.52	158.10	×35
High	6.40	710.68	×111

ulation quality of at least engineering-precision should be considered for such purposes.

Using ChromaTech, the quality of the simulation is improved by increasing the number of elements N_e^z for fixed axial polynomial orders $N^z \in \{3, 4\}$. The radial polynomial order N^r is varied such that axial approximation errors are dominating over the radial errors, i.e. radial polynomial orders $N^r \in \{6, \ldots, 12\}$ are used depending on the accuracy of the axial discretization. When using CADET, the spatial discretization parameters available to control the quality of the simulation are the number of finite volume elements in the mobile N_e^z and pore N_e^r phases. A fixed ratio of $N_e^z = 2^k$, $N_e^r = 2^{k-1}$, $k = 4, \ldots, 9$ is used in the following since it gives the best performance on this case (results are not shown).

Fig. 7(a) shows the comparisons of both codes in terms of discrete problem size with the data summarized in Table. 4. The comparisons shows, that ChromaTech is able to reduce the discrete problem size compared to CADET by a factor of ×30, ×59, and ×121, when a simulation quality of low-, engineering- and high-precision is required, respectively.

Although the convergence properties of the spectral engine used within ChromaTech are impressive, it is often the computational cost which is the decisive criterion for choosing between different simulation strategies. In Fig. 7(b), the results of the comparisons between the two codes, in terms of the computational cost measured in wall clock time, are shown. Here, CADET has been used with multiple CPU threads, taking advantage of its parallel implementation, to reduce compute time. ChromaTech has been implemented on a single CPU core, and a full parallelization strategy is beyond the scope of this work. The two codes are compared on a single CPU core to provide the most fair basis for comparing the efficiency of the methods applied, instead of their implementation. The results of the comparisons are summarized in Table 5. They demonstrate, that ChromaTech can reduce the compute time by a factor of ×21, ×51 and ×111, to achieve simulations of low-, engineering- and high-precision quality, respectively.

Comparing Tables 4 and 5 shows, that the compute times scales linearly with the discrete problem size for CADET. This indicates that the finite volume method

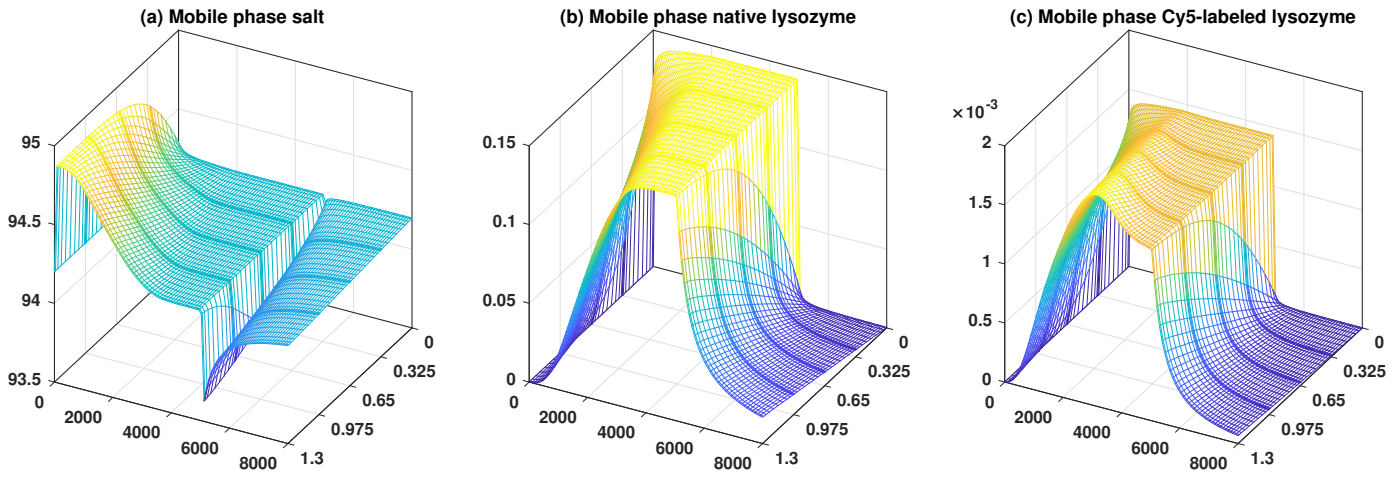

Figure 8: Mobile phase concentrations as a function of time and axial column position of (a) salt (b) native lysozyme and (c) Cy5-labeled lysozyme. The z-axis is concentration ($\mathrm{mol\,m^{-3}}$), the x-axis is time (s) and the y-axis is axial column position (m). The model parameters taken from von Lieres and Andersson (2010) are given in Table 3.

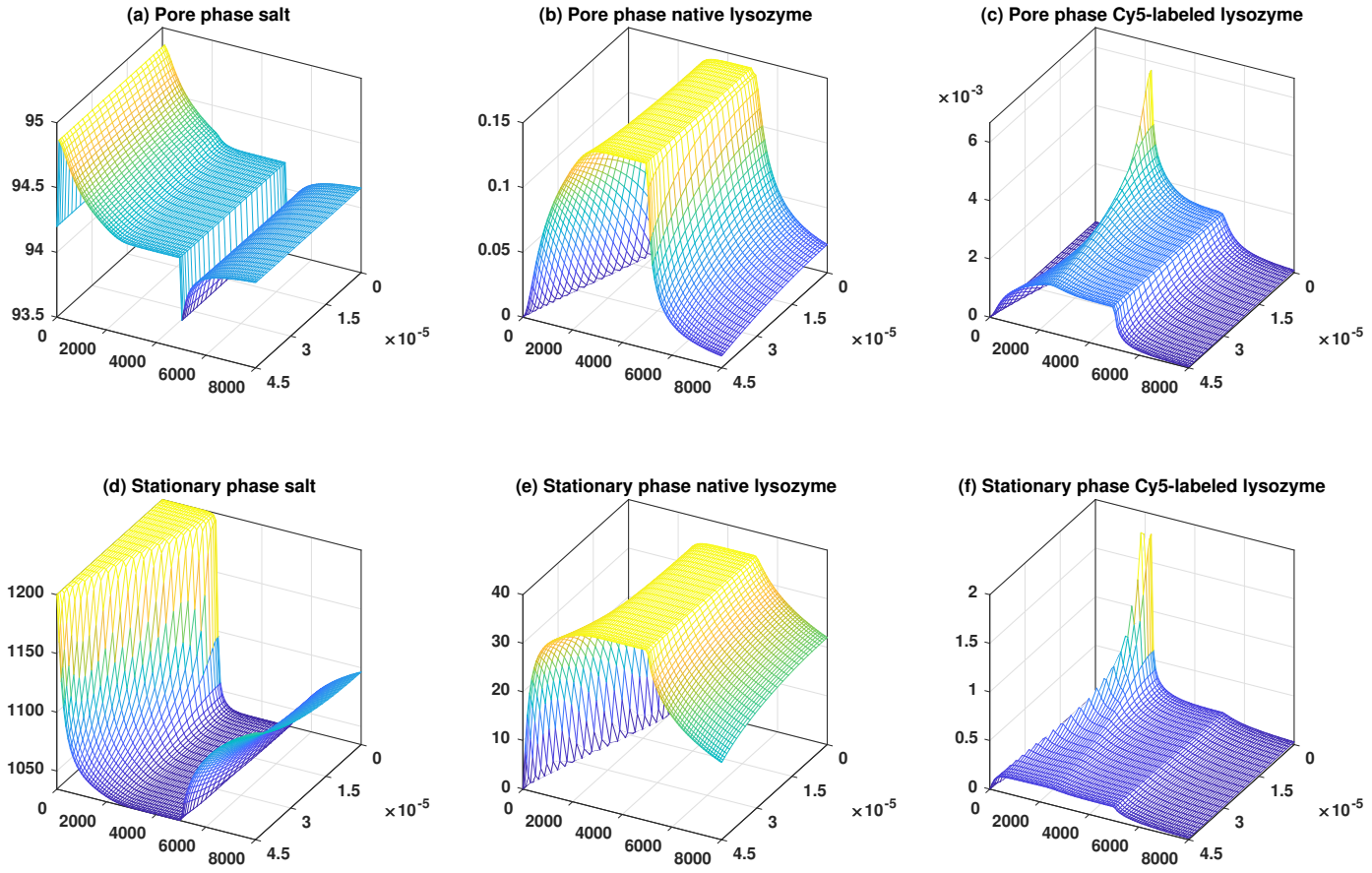

Figure 9: Pore phase (a)-(c) and stationary phase (d)-(f) concentrations of salt, native lysozyme and Cy5-labeled lysozyme as a function of time and radial column position inside a bead at an axial column position of $z = 0.58$. The z-axis is concentration ($\mathrm{mol\,m^{-3}}$), the x-axis is time (s) and the y-axis is radial column position (m). The model parameters taken from von Lieres and Andersson (2010) are given in Table 3.

implemented in CADET is dedicated and highly efficient. That is a result of solving linear systems by a domain decomposition method as previously discussed in section 3.7.

5.3. Case 3: Performance benchmark for high load volume

The last case considered is the hardest and most demanding to solve due to the presence of very steep concentration fronts resulting from non-linear adsorption dynamics. The purpose is to demonstrate, that ChromaT-

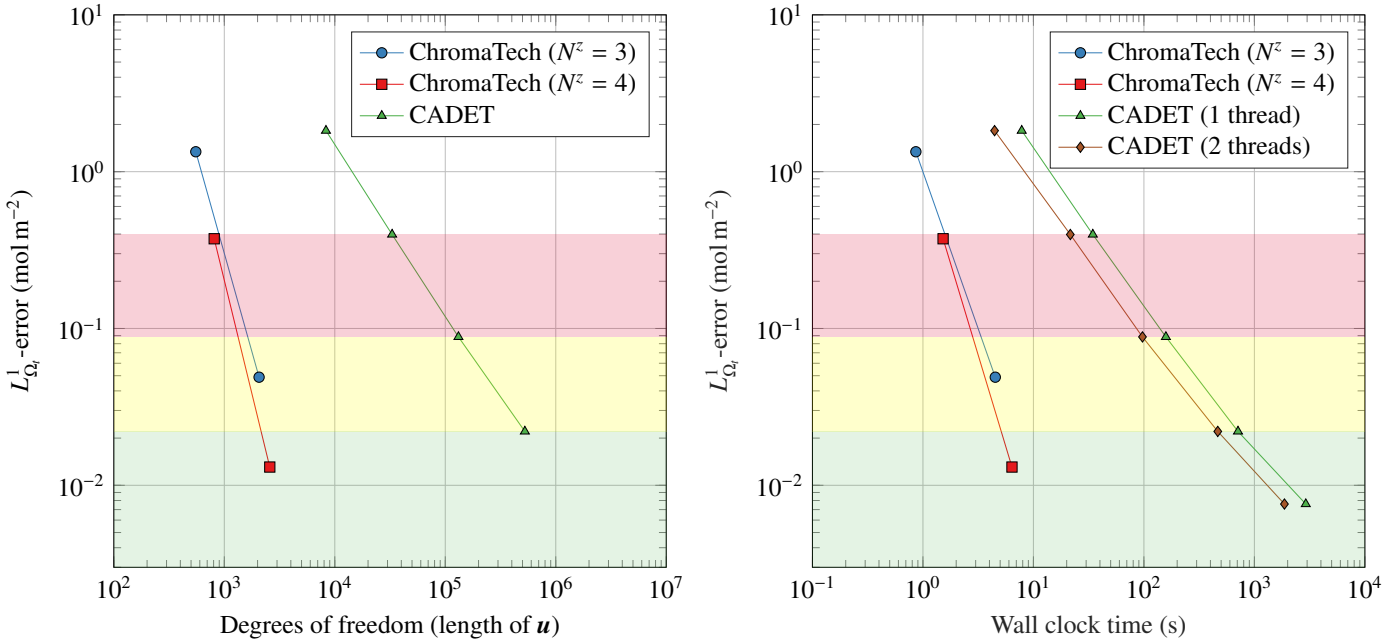

(a) Approximation error against discrete problem size

(b) Approximation error against compute time

Figure 10: The $L^1_{\Omega_t}$-error against computational work in (a) discrete problem size and (b) computational cost measured in wall clock time for the performance benchmark using high load volume (section 5.3). The results are shown in logarithmic scale.

ech is stable and to measure its performance by comparing against CADET.

The case is taken from von Lieres and Andersson (2010) with detailed model parameters listed in Table 6. The goal is to separate a two component feed mixture of native lysozyme and Cy5-labeled lysozyme. Note that the feed concentration of Cy5-labeled lysozyme is one hundred times lower than native lysozyme. Moreover, the feed mixture is injected at the column inlet for a long time of $t_{\text{inj}} = 5000$ s giving rise to non-linear adsorption dynamics. The feed mixture is loaded onto a column that has been pre-equilibrated with running salt buffer with concentration $c_{0,\text{init}} = 94.2\ \text{mol}\,\text{m}^{-3}$. This salt concentration is maintained during the entire numerical experiment. Moreover, surface diffusion is assumed to be negligible, i.e. $D_{s,i} = 0$, $\forall i = 0, \ldots, N_c$.

Fig. 8 shows a simulation of the mobile phase concentrations over time for all axial column positions. Notice the sharp concentration fronts in the salt profile in Fig. 8(a) and the concentration overshoots of Cy5-labeled lysozyme in (c).

A simulation of the pore phase and stationary phase concentrations for a representative bead at an axial column position of $z = 0.58$ cm is shown in Fig. 9. The concentrations are shown over time for all radial column positions. As in the mobile phase, the salt concentration profile is steep within the pore phase. Moreover, concentration overshoots are observed inside the pore and stationary phases for Cy5-labeled lysozyme.

The observed concentration overshoots are a consequence of competitive binding between native and labeled lysozyme. Such concentration overshoots inside chromatography beads have also been experimentally observed (Teske et al., 2006).

The simulation results demonstrate, that ChromaTech can simulate non-linear chromatographic processes with steep concentration fronts without compromising stability. That is because the discontinuous Galerkin method has strong build-in stability properties (Hesthaven and Warburton, 2008).

The performance of ChromaTech is tested by benchmarking against CADET. A high-precision reference solution $\boldsymbol{u}_{\text{ref}}$ is obtained using ChromaTech ($N^z_e = 10$, $N^z = 10$, $N^r = 35$). Simulations are obtained with ChromaTech using discretization parameters $N^z \in \{3, 4\}$, $N^z_e \in \{2, 4\}$, $N^r \in \{10, 20\}$. For CADET, a ratio between finite volume elements in the mobile and pore phases of $N^z_e = 2^k$, $N^r_e = 2^k$, $k = 5, \ldots, 9$ is used since its gives the best performance on this case (results are not shown). Both ChromaTech and CADET are run with absolute and relative time integration tolerances of 10^{-6} and 10^{-8}, respectively.

Fig. 10 and Tables 7 and 8 summarize the results of the comparisons. The results demonstrate, that ChromaTech can reduce the discrete problem size by a factor of ×41, ×64, ×204 when a simulation quality of low-, engineering- and high-precision is required, respectively. Moreover, ChromaTech can compute with a factor of ×23, ×35 and ×111 faster compared to CADET on a single CPU thread when a simulation quality of low-, engineering- and high-precision is required, respectively.

6. Conclusions

In this work, the ChromaTech framework has been presented for simulation of liquid chromatography processes with mass transport modelled by the pore and surface diffusion general rate model. ChromaTech is based on a highly efficient spatial discretization procedure that achieves exponential decay of approximation errors within axial and radial elements while maintaining stability.

ChromaTech's spectral engine has been validated on a simple problem involving a single-component feed mixture under linear adsorption conditions. Here, simulations were compared with a high-precision reference obtained using CADET-semi-analytic, a code which is based on the numerical inverse Laplace operator with a proven truncation error at the column outlet.

The performance of ChromaTech was evaluated in multicomponent protein purification cases with both linear and non-linear adsorption dynamics. Here, ChromaTech was compared against CADET, a dedicated code based on a finite volume method with second (low) order spatial accuracy. Since no analytical solution is available for non-linear chromatography models, a fully resolved reference solution was used for comparisons instead. It was demonstrated, that ChromaTech and CADET gives similar chromatograms, providing evidence that both codes are correctly implemented. However, ChromaTech can significantly reduce computational efforts in terms of both computational cost and discrete problem size without compromising stability. Therefore, it is especially suitable as a building block in more advanced model-based strategies including:

- Efficient monitoring of chromatography columns based on non-linear state-estimation.
- Efficient process control using non-linear model predictive control.
- Efficient downstream flow-sheet designs using rigorous process synthesis tools.
- Rigorous uncertainty analysis using e.g. the Bayesian inference framework.

7. Acknowledgement

The project received financial support from Innovation Fund Denmark through the BIOPRO2 strategic research centre (Grant number 4105-00020B).

References

Ahmed, I., Kaspar, B., Sharma, U., 2012. Biosimilars: Impact of biologic product life cycle and european experience on the regulatory trajectory in the united states. Clinical Therapeutics 34, 400–419.

Atkins, P., de Paula, J., 1998. Physical chemistry. Ninth ed., Freeman, New York.

Bassi, F., Rebay, S., 1997. A high-order accurate discontinuous finite element method for the numerical solution of the compressible Navier-Stokes equations. Journal of Computational Physics 131, 267–279.

Brenan, K.E., Campbell, S.L., Petzold, L.R., 1996. Numerical solution of initial-value problems in differential-algebraic equations. SIAM, Philadelphia, PA.

Briskot, T., Stückler, F., Wittkopp, F., Williams, C., Yang, J., Konrad, S., Doninger, K., Griesbach, J., Bennecke, M., Hepbildikler, S., Hubbuch, J., 2019. Prediction uncertainty assessment of chromatography models using Bayesian inference. Journal of Chromatography A 1587, 101–110.

Brooks, C.A., Cramer, S.M., 1992. Steric mass-action ion exchange: Displacement profiles and induced salt gradients. AIChE Journal 38, 1969–1978.

Cazap, E., Jacobs, I., McBride, A., Popovian, R., Sikora, K., 2018. Global Acceptance of Biosimilars: Importance of Regulatory Consistency, Education, and Trust. The Oncologist 23, 1188–1198.

Cherny, N., Sullivan, R., Torode, J., Saar, M., Eniu, A., 2016. ESMO European Consortium Study on the availability, out-of-pocket costs and accessibility of antineoplastic medicines in Europe. Annals of Oncology 27, 1423–1443.

Close, E.J., Salm, J.R., Bracewell, D.G., Sorensen, E., 2014. A model based approach for identifying robust operating conditions for industrial chromatography with process variability. Chemical Engineering Science 116, 284–295.

CMake, 2019. http://cmake.org.

Costa, C., Rodrigues, A., 1985a. Design of cyclic fixed-bed adsorption processes. part 1: Phenol adsorption on polymeric adsorbents. Aiche Journal 31, 1645–1654.

Costa, C., Rodrigues, A., 1985b. Intraparticle diffusion of phenol in marcoreticular adsorbents: modelling and experimental study of batch and cstr adsorbers. Chemical Engineering Science 40, 983–993.

Danckwerts, P., 1953. Continuous flow systems. Chemical Engineering Science 2, 1–13.

Demmel, J.W., Eisenstat, S.C., Gilbert, J.R., Li, X.S., Liu, J.W.H., 1999a. A supernodal approach to sparse partial pivoting. SIAM Journal on Matrix Analysis and Applications 20, 720–755.

Demmel, J.W., Gilbert, J.R., Li, X.S., 1999b. An asynchronous parallel supernodal algorithm for sparse gaussian elimination. Siam Journal on Matrix Analysis and Applications 20, 915–952.

Douglas, J., Dupont, T., 1976. Interior penalty procedures for elliptic and parabolic Galerkin methods, in: Glowinski, R., Lions, J.L. (Eds.), Computing Methods in Applied Sciences. Lecture Notes in Physics. Springer, Berlin, Heidelberg. volume 58, pp. 207–216.

Douglas, N.A., Brezzi, F., Cockburn, B., Marini, L.D., 2002. Unified analysis of discontinuous Galerkin methods for elliptic problems. Siam Journal on Numerical Analysis 39, 1749–1779.

Dumbser, M., Balsara, D.S., Toro, E.F., Munz, C.E., 2008. A unified framework for the construction of one-step finite volume and discontinuous galerkin schemes on unstructured meshes. Journal of Computational Physics 227, 8209–8253.

Engell, S., 2007. Feedback control for optimal process operation. Journal of Process Control 17, 203–219.

Engsig-Karup, A.P., Eskilsson, C., Bigoni, D., 2016. A stabilised nodal spectral element method for fully nonlinear water waves. Journal of Computational Physics 318, 1–21.

Farid, S.S., 2007. Process economics of industrial monoclonal antibody manufacture. Journal of Chromatography B: Analytical Technologies in the Biomedical and Life Sciences 848, 8–18.

Feidl, F., Vogg, S., Wolf, M., Podobnik, M., Ruggeri, C., Ulmer, N., Wälchli, R., Souquet, J., Broly, H., Butté, A., Morbidelli, M., 2020. Process-wide control and automation of an integrated continuous manufacturing platform for antibodies. Biotechnology and Bioengineering 117, 1367–1380.

Gaël, G., Benoît, J., et al., 2010. Eigen v3. http://eigen.tuxfamily.org.

Gassner, G.J., Beck, A.D., 2013. On the accuracy of high-order discretizations for underresolved turbulence simulations. Theoretical and Computational Fluid Dynamics 27, 221–237.

Gerontas, S., Shapiro, M.S., Bracewell, D.G., 2013. Chromatography modelling to describe protein adsorption at bead level. Journal of Chromatography A 1284, 44–52.

Gomis-Fons, J., Schwarz, H., Zhang, L., Andersson, N., Nilsson, B., Castan, A., Solbrand, A., Stevenson, J., Chotteau, V., 2020. Model-based design and control of a small-scale integrated continuous end-to-end mab platform. Biotechnology Progress , e2995.

Hanke, A.T., Ottens, M., 2014. Purifying biopharmaceuticals: Knowledge-based chromatographic process development. Trends in Biotechnology 32, 210–220.

Hesthaven, J.S., 1998. From electrostatics to almost optimal nodal sets for polynomial interpolation in a simplex. SIAM Journal on Numerical Analysis 35, 655–676.

Hesthaven, J.S., Warburton, T., 2002. Nodal high-order methods on unstructured grids: I. Time-domain solution of Maxwell's equations. Journal of Computational Physics 181, 186–221.

Hesthaven, J.S., Warburton, T., 2008. Nodal Discontinuous Galerkin Methods: Algorithms, Analysis, and Applications, in: Texts in Applied Mathematics. Springer, New York, NY. volume 54, pp. 1–501.

Hindmarsh, A.C., Brown, P.N., Grant, K.E., Lee, S.L., Serban, R., Shumaker, D.E., Woodward, C.S., 2005. SUNDIALS: Suite of nonlinear and differential/algebraic equation solvers. ACM Transactions on Mathematical Software 31, 363–396.

Holmqvist, A., Magnusson, F., 2016. Open-loop optimal control of batch chromatographic separation processes using direct collocation. Journal of Process Control 46, 55–74.

Hørsholt, A., Christiansen, L.H., Meyer, K., Huusom, J.K., Jørgensen, J.B., 2019a. Spatial discretization and kalman filtering for ideal packed-bed chromatography. Proceedings of the 18th European Control Conference (ECC) , 2356–2361.

Hørsholt, A., Christiansen, L.H., Ritschel, T.K., Meyer, K., Huusom, J.K., Jørgensen, J.B., 2019b. State and input estimation of nonlinear chromatographic processes. 2019 IEEE Conference on Control Technology and Applications (CCTA) , 1030–1035.

Huusom, J.K., 2015. Challenges and opportunities in integration of design and control. Computers and Chemical Engineering 81, 138–146.

Kozlowski, S., Woodcock, J., Midthun, K., Sherman, R.B., 2011. Developing the nation's biosimilars program. New England Journal of Medicine 365, 385–388.

Lee, J.H., 2011. Model predictive control: Review of the three decades of development. International Journal of Control, Automation and Systems 9, 415–424.

Leweke, S., von Lieres, E., 2016. Fast arbitrary order moments and arbitrary precision solution of the general rate model of column liquid chromatography with linear isotherm. Computers and Chemical Engineering 84, 350–362.

Leweke, S., von Lieres, E., 2018. Chromatography Analysis and Design Toolkit (CADET). Computers and Chemical Engineering 113, 274–294.

von Lieres, E., Andersson, J., 2010. A fast and accurate solver for the general rate model of column liquid chromatography. Computers and Chemical Engineering 34, 1180–1191.

LLVM, 2019. http://llvm.org/.

Ma, Z., Whitley, R.D., Wang, N.H.L., 1996. Pore and surface diffusion in multicomponent adsorption and liquid chromatography systems. AIChE Journal 42, 1244–1262.

McGlaughlin, M.S., 2012. An emerging answer to the downstream bottleneck. Bioprocess International 10, 58–61.

Meyer, K., 2020. Advanced simulation of preparative chromatography processes. Ph.D. thesis. Technical University of Denmark.

Meyer, K., Bisgaard, T., Huusom, J.K., Abildskov, J., 2017. Supervisory model predictive control of the heat integrated distillation column. Ifac-papersonline 50, 7375–7380.

Meyer, K., Huusom, J.K., Abildskov, J., 2018a. Efficient implicit-explicit time stepping for accurate and rapid simulation of chromatographic models. Computer Aided Chemical Engineering 44, 853–858.

Meyer, K., Huusom, J.K., Abildskov, J., 2018b. High-order approximation of chromatographic models using a nodal discontinuous Galerkin approach. Computers and Chemical Engineering 109, 68–76.

Meyer, K., Huusom, J.K., Abildskov, J., 2019. A stabilized nodal spectral solver for liquid chromatography models. Computers and Chemical Engineering 124, 172–183.

Miyabe, K., 2014. Moment equations for chromatography based on Langmuir type reaction kinetics. Journal of Chromatography A 1356, 171–179.

Monk, B.J., Lammers, P.E., Cartwright, T., Jacobs, I., 2017. Barriers to the access of bevacizumab in patients with solid tumors and the potential impact of biosimilars: A physician survey. Pharmaceuticals 10, 19.

Nargund, S., Guenther, K., Mauch, K., 2019. The move toward biopharma 4.0. Genetic Engineering and Biotechnology News 39, 53–55.

Nfor, B.K., Verhaert, P.D.E.M., van der Wielen, L.A.M., Hubbuch, J., Ottens, M., 2009. Rational and systematic protein purification process development: the next generation. Trends in Biotechnology 27, 673–679.

Palm, J., Eskilsson, C., Bergdahl, L., 2017. An hp-adaptive discontinuous galerkin method for modelling snap loads in mooring cables. Ocean Engineering 144, 266–276.

Papathanasiou, M.M., Steinebach, F., Morbidelli, M., Mantalaris, A., Pistikopoulos, F.N., 2017. Intelligent, model-based control towards the intensification of downstream processes. Computers and Chemical Engineering 105, 173–184.

Pirrung, S.M., Berends, C., Backx, A.H., van Beckhoven, R.F.W.C., Eppink, M.H.M., Ottens, M., 2019. Model-based optimization of integrated purification sequences for biopharmaceuticals. Chemical Engineering Science: X 3, 100025.

Pirrung, S.M., van der Wielen, L.A., van Beckhoven, R.F., van de Sandt, E.J., Eppink, M.H., Ottens, M., 2017. Optimization of biopharmaceutical downstream processes supported by mechanistic models and artificial neural networks. Biotechnology Progress 33, 696–707.

Püttmann, A., Nicolai, M., Behr, M., von Lieres, E., 2014. Stabilized space-time finite elements for high-definition simulation of packed bed chromatography. Finite Elements in Analysis and Design 86, 1–11.

Püttmann, A., Schnittert, S., Naumann, U., von Lieres, E., 2013. Fast and accurate parameter sensitivities for the general rate model of column liquid chromatography. Computers and Chemical Engineering 56, 46–57.

Qamar, S., Abbasi, J.N., Javeed, S., Seidel-Morgenstern, A., 2014. Analytical solutions and moment analysis of general rate model for linear liquid chromatography. Chemical Engineering Science 107, 192–205.

Qamar, S., Uche, D.U., Khan, F.U., Seidel-Morgenstern, A., 2017. Analysis of linear two-dimensional general rate model for chromatographic columns of cylindrical geometry. Journal of Chromatography A 1496, 92–104.

Rathore, A.S., Kumar, D., Kateja, N., 2018. Recent developments in chromatographic purification of biopharmaceuticals. Biotechnology Letters 40, 895–905.

Rodrigues, A.E., 1984. Percolation theory I-basic principles and II-modeling and design of percolation columns, in: Chromatography, Percolation, Adsorption and Gas adsorption. AIChE. volume 5 of AIChEMI series B: Stagewise and mass transfer operations, pp. 7–24.

Sanchez-Garcia, L., Martín, L., Mangues, R., Ferrer-Miralles, N., Vázquez, E., Villaverde, A., 2016. Recombinant pharmaceuticals from microbial cells: A 2015 update. Microbial Cell Factories 15, 33.

Schmidt-Traub, H., Schulte, M., Seidel-Morgenstern, A. (Eds.), 2012. Preparative Chromatography. 2 ed., Wiley-VCH Verlag GmbH & Co. KGaA, Weinheim, Germany.

Teske, C.A., Lieres, E.v., Schröder, M., Ladiwala, A., Cramer, S.M., Hubbuch, J.J., 2006. Competitive adsorption of labeled and native protein in confocal laser scanning microscopy. Biotechnology and Bioengineering 95, 58–66.

Walsh, G., 2018. Biopharmaceutical benchmarks 2018. Nature

Biotechnology 36, 1136–1145.
Xu, H., Cantwell, C.D., Monteserin, C., Eskilsson, C., Engsig-karup, A.P., Sherwin, S.J., 2018. Spectral/hp element methods: Recent developments, applications, and perspectives. Journal of Hydrodynamics 30, 1–22.